UCLouvain

epl

École polytechnique de Louvain

Porous short fiber reinforced composites

Full-field implementation and evaluation of several homogenization strategies

Author: **Julien Demey**
Supervisors: **Issam Doghri, Chiheb Naili**
Readers: **Laurent Adam, Laurent Delannay**
Academic year 2018–2019
Master [120] in Mechanical Engineering

Acknowledgements

I would like to deeply thank Pr. Issam Doghri for his interesting discussions and precious advices. It was an honor for me to work with someone so passionated by his work. Thanks for offering me the great opportunity to work directly in the office and be part of the team.

I would also thank Chiheb Naili for his time and explanations for the past few months. No matter the time, you always were ready to help, so thank you very much.

Finally I would like to thank the team of e-Xstream engineering for the support and numerous advices and free access to their software.

Julien.

Contents

List of Figures

List of Tables

Abstract

This master thesis deals with the evaluation of several homogenization methods for short-fiber reinforced composites (SFRC) using micro-mechanical modeling. By means of several numerical homogenization schemes we computed the macroscopic response of the material to compare and evaluate the best modeling strategy against reference full-field finite elements (FE) simulations on unit cells. Firstly we studied the homogenization of porous unidirectional (UD) SFRCs using three FE models : RVE, UD unit cell and a two-level decomposition of the unit cell. Secondly we considered porous misaligned SFRCs and investigated three homogenization approaches : a direct FE homogenization using an RVE, a two-step method in which the first step is based on FE homogenization of the porous UD unit cell and the second step performed with three homogenization schemes : either Voigt, Reuss or a method inspired by the Mori-Tanaka model using only FE results, and finally we coupled the two-step method with a two-level decomposition of the porous UD pseudo-grain during the first step of the procedure. Results from two-step method using direct FEA of three-phase pseudo-grains (PGs) and FE-MT shows better agreement with RVE reference results. Only linear elasticity is considered in the present work. We used Python scripts to generate the models in the FE solver Abaqus (2019) and post-process the macro response of the material.

Keywords :
Porous composites, Short fiber-reinforced composite, Homogenization, Linear elasticity, Finite elements

Introduction

Short-fiber reinforced composites (SFRC) have been and still are today of a sustained interest in many industrial applications. Because they have a light weight, improve mechanical properties and have low fabrication costs. It combines enhanced stiffness of the fibers with all the attractive properties of thermoplastics or thermoset materials.

SFRC parts, usually glass fibers embedded in a thermoplastic polymer, are often mass-produced by injection molding, which reduces the cycle time and results in an automatic processing that enables a large scale production. Injection molding produces various fiber filled parts in high volumes for applications in the aerospace industry, automotive industry, medical products, sporting goods etc. Injection molding of glass fiber-reinforced composites has the capability of producing near net shape articles having exceptional physical and mechanical properties. The process typically employs a reciprocating single-screw extrusion machine, as shown schematically in Figure 1.

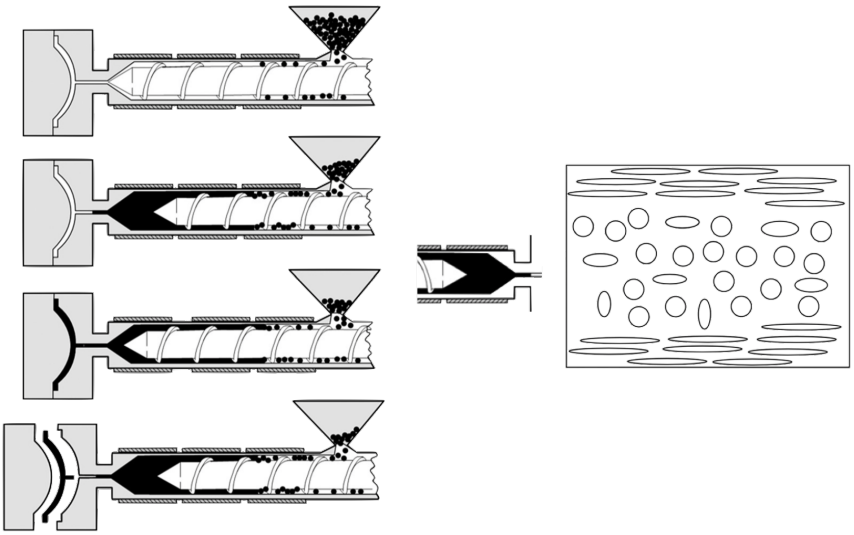

Figure 1: Fiber orientation in injection molded parts (from Liu (2012))

On the one hand most manufacturing processes give rise to micro-geometries in which the fibers are neither perfectly aligned nor fully random but show orientation distribution between these two extremes. In the case of injection-molded parts made of short-fiber reinforced plastics, the short-fibers are oriented themselves due to the flow and interact with the neighboring fibers and the wall. Variation of fiber orientation are usually observed through the thin skin and the core (right figure on Figure 1). Therefore the mechanical and physical properties of the end products highly depend on the fibers orientation. The molding of such short-fiber composites are reviewed in Advani and Hsiao (2012).

On the other hand voids are one of the most common types of defects induced by the manufacturing process in SFRC materials. The presence of such defects has an influence on the material properties (Prakash (1981)) but still can be reduced using well-chosen process parameters.

Under such orientation distribution of the fibers and the presence of voids the material response appears to be anisotropic and heterogeneous throughout the part. Therefore to compute the macro stress and strain fields within the composite micro-mechanical approaches have been developed as it enables us to evaluate the micro-response of each phase. Among analytical and/or numerical methods we could use full-field methods, e.g. finite elements (FE), to solve representative volume element (RVE) problems to investigate the effective elastic properties of such composites. However the direct FE approach becomes costly in the case of complex micro-structures, e.g. containing a large number of fibers with different orientations, even more when we consider high fiber volume fractions and aspect ratios. So, mean-field homogenization (MFH) methods have been developed to give computationally cheaper but still satisfying results. For instance, Mori-Tanaka (MT) model (Mori and Tanaka (1973)) and interpolative double inclusion (DI) model proposed by Lielens et al. (1998) both give accurate results when considering composites where all the fibers have the same material properties, shapes, aspect ratio and orientation. Nevertheless, due to the anisotropy caused by misalignment and the non-random orientation distribution of the fibers abovementioned MFH models (such as MT of DI) need to be enhanced. A well-used method from Benveniste (1987) has been widely applied to numerous studied cases but it does lead to non-symmetric overall stiffness tensor and so physically unacceptable results as it considers isotropic constituents with randomly oriented ellipsoidal particles.

For misaligned SFRCs one solution advocated by Pierard et al. (2004) and Doghri and Friebel (2005) which commonly used ever since in the literature is the two-step homogenization procedure. The RVE is decomposed into a set of UD pseudo-grains (PG). Each PG is a two-phase material composed of aligned identical fibers embedded in the matrix. First, each PG is homogenized by means of a MF model, typically Mori-Tanaka. Then, in a second step, the RVE is seen as an aggregate of PGs and is homogenized with a MF model, typically Voigt (1889) or Reuss (1929). Finally we will pair the two-step method with a two-level decomposition FE homogenization of each PG during the first step and compare it with the aforementioned direct FE homogenization of the classical two-step procedure.

This present work aims at studying various homogenization methods using only full-field FE simulations, e.g. no MF models. The main goal is to study the case of SFRCs with porosity, first considering aligned short-fibers and then misaligned short-fibers. We will study fiber volume fractions from $v_f = 10\%$ up to 30% and voids volume fractions ranging $v_p = 1\%$ to 10%.

Chapter 1 defines some important concepts regarding the scale transition methods. Chapter 2 recalls full-field FE homogenization theory and explain the modeling process of the models we used in Abaqus (2019). Chapters 3 and 4 study, explain and compare the homogenization methods proposed in this work for both non-porous and porous SFRCs in the case of aligned and misaligned fibers orientation, respectively.

Unless specified otherwise, the following convention has been adopted : scalar and vectors are denoted by lower case letters (i.e. a) and boldfaced lower case latin letters (i.e. $\boldsymbol{a}$), respectively; fourth orders tensors are denoted by boldfaced upper case latin letters (i.e. $\boldsymbol{C}$, $\boldsymbol{A}$).

Chapter 1

Scale transition methods

1 Heterogeneous materials

Numerous engineering materials are considered as heterogeneous in the sense that they are composed of a certain number of constituents (the phases) that differ from each other according to the length scale at which they are observed. Each phase differs from the others by its own physical and mechanical properties. The behavior of such so-called composite materials is imposed by the mechanical properties specific to each phase and the disposition of the microstructure inside the composite (the orientation of the fibers etc.). Note that each constituent might be seen as heterogeneous depending on the scale we consider it (see Böhm (2019) for more information).

2 Scale separation

Classically in homogenization techniques we aim at replacing the heterogeneous medium by a fictitious homogeneous one which behaves globally in the same way. Following Aboudi (1991), the relevant scales at which continuum mechanics are applicable are :

- Micro-scale : lowest length scale described by a given micromechanical model (constituent level)
- Meso-scale : intermediate length scale (laminate, composite level)
- Macro-scale : highest length scale described by a given micromechanical model (global/structural level)

The behavior of an inhomogeneous material is described by several fields : stress field $\boldsymbol{\sigma}(x)$, strain field $\boldsymbol{\varepsilon}(x)$ and the displacements field $\mathbf{u}(\mathbf{x})$. These fields are split into different contributions related to the length scales, the so-called micro-, macro- and meso-fields.
The length scales in a given material are assumed to be well separated in most micro-mechanical models. The splitting of the fields can formally be written as :

$$\boldsymbol{\varepsilon}(x) = \langle \boldsymbol{\varepsilon} \rangle + \boldsymbol{\varepsilon}'(x) \tag{1.1}$$

$$\boldsymbol{\sigma}(x) = \langle \boldsymbol{\sigma} \rangle + \boldsymbol{\sigma}'(x) \tag{1.2}$$

with $\langle \boldsymbol{\varepsilon} \rangle$ and $\langle \boldsymbol{\sigma} \rangle$ the macroscopic averaged fields, $\boldsymbol{\varepsilon}'(x)$ and $\boldsymbol{\sigma}'(x)$ the microscopic fluctuations.

This is now understood that modeleling the behavior of material depends on the scale from which it is considered. For instance, if we consider a structure of composite material it can be seen on the one hand as made of a homogeneous material at the macroscopic point of view. On the other hand at each macroscopic point, local stress and strain relations depend on the microstructure of the material which

is heterogeneous at the microscopic scale. For this reason, to take into account the heterogeneities of the microstructure we define a so-called "representative volume element" (RVE) at each macroscopic point (see section 3).

We can define various length scales based on Zaoui (2002) to operate correctly the scale separation. So :

- d_0 : lower length bound under which continuum mechanics is no more valid
- d : characteristic length of the considered inhomogeneities
- l : characteristic size of the RVE
- λ : fluctuation length of the prescribed mechanical loading
- L : characteristic size of the structure

The size of the RVE must be much smaller than the one of the structure ($l \ll L$) to consider the structure as a continuum medium. Moreover characteristic size of the heterogeneities and deformation mechanisms must be sufficiently small compared to RVE size so that the volume element can be considered as representative of the studied material, whatever its location in the macroscopically homogeneous body. Furthermore the condition $d_0 \ll d$ guarantees the validity of continuum mechanics at the scale of the RVE. One last condition $l \ll \lambda$ states that the size of the RVE must be much smaller than the fluctuation length of the prescribed mechanical loading of the whole body so as to make possible the use of classical integral and differential tools of structural analysis.

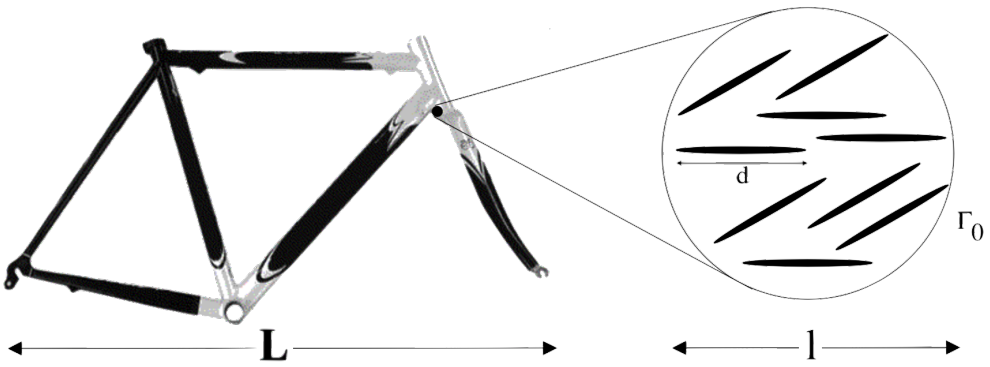

Figure 1.1: Length scales separation. Left side : the structure is considered as homogeneous at the macroscopic level. Right side : at the RVE level we can see heterogeneities. From Pierard (2006).

3 Representative Volume Element (RVE)

As introduced here above, micro-mechanics account for a material's heterogeneous microstructure while allowing to consider it as an effective or pseudo-homogeneous continuum at a higher scale. The link between the microscopic scale (that of the heterogeneities) and the macroscopic one (where the solid can be seen as locally homogeneous) is made via the concept of representative volume element (RVE). Micro-mechanics relies also on repeating unit cell (RUC) (more information in Aboudi et al. (2012)).

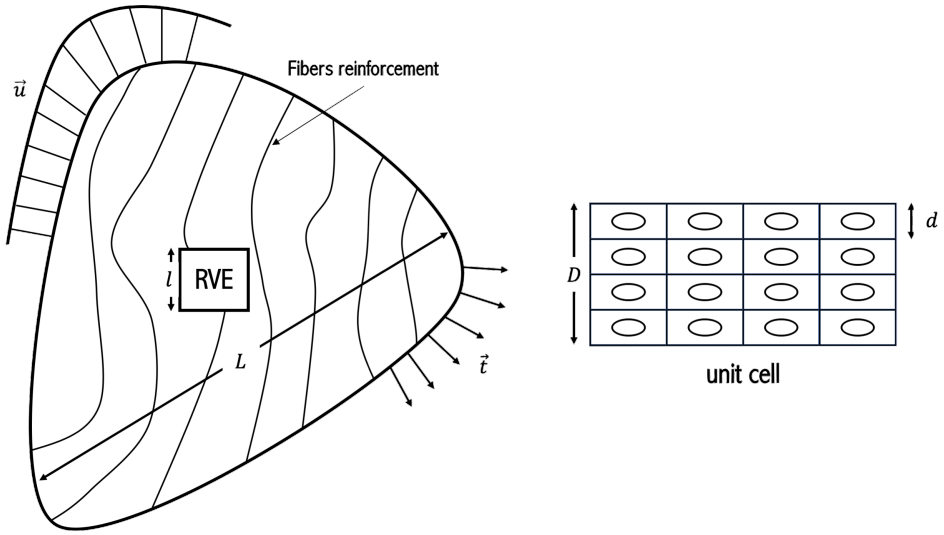

Figure 1.2: Length scales from the structure of characteristic length L to the RVE of size l and the RUC of size d. Vectors $\boldsymbol{u}$ and $\boldsymbol{t}$ respectively stand for the applied displacement field and the applied stress field. *(Note that* $\frac{D}{L} \ll 1$ *and* $\frac{d}{D} \ll 1$*)*

Left side on Figure 1.2 represent an RVE. Each macroscopic point can be seen as the center of such RVE. It is defined as a statistically homogeneous material sufficiently accurate to represent the mean constitutive response of the material as a whole. In other words this is a sample of the composite material that is structurally entirely typical of the whole composite on average, and contains a sufficient number of material phases to represent the microstructure, i.e. it should be sufficiently large enough compared to the scales of the microstructure (in general four to five times the characteristic length of the heterogeneities), but still small compared to the entire structure. For instance, for a fictitious perfectly homogeneous material, the RVE would be infinitely small.

Equivalently the heterogeneous microstructure can be approximated as periodic, where the RUC (right side on Figure 1.2) is a volume of material that repeats itself periodically to model the overall microstructure. The repeating aspect of the RUC is imposed by periodic boundary conditions. Because it is often difficult to ensure the chosen analysis volume to be actually an RVE, the periodicity approach of the RVE is usually utilized.

3.1 Boundary Conditions

Generally for any given periodic phase arrangement unit cells are non-unique and the range of possible shapes is especially wide (see Figure 1.3) when symmetries are present in the micro-geometry.

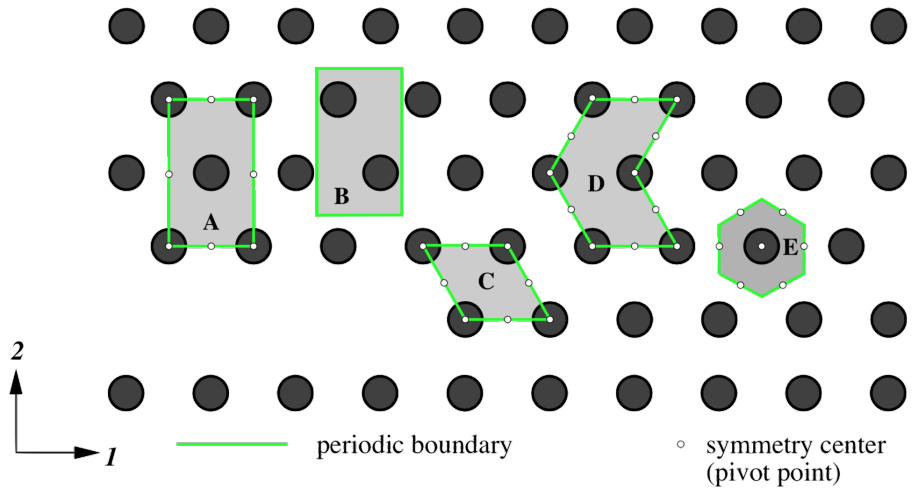

Figure 1.3: Periodic hexagonal array of circular inhomogeneities in a matrix : examples of cells that can be used to describe the mechanical response of the phase arrangement. From Böhm (2019).

.

Several types of boundary conditions can be imposed on the RVE. Among them : prescribed displacements, prescribed tractions and periodic boundary conditions. The latter will be developed in what follows[1].

Periodic boundary conditions generally lead to an intermediate and more accurate response which makes possible for the cell size to be considered smaller (see Figure 1.4).

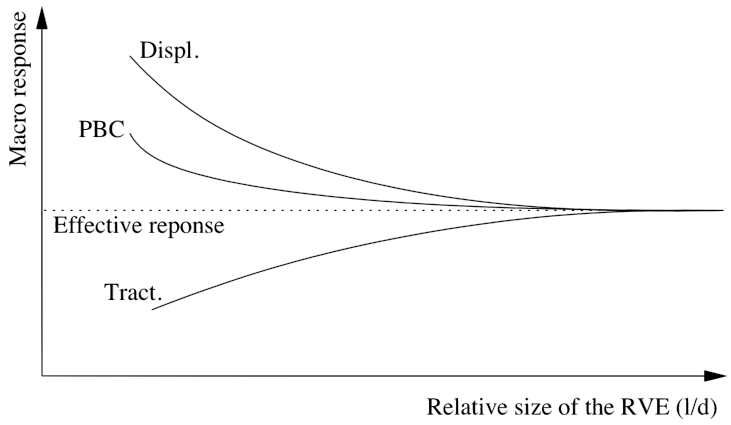

Figure 1.4: Advantage of periodic boundary conditions regarding the accuracy of the predictions with respect to the RVE size compared to other boundary conditions (Displ. : prescribed linear displacements, PBC : periodic boundary conditions, Tract. : prescribed uniform traction). From Pierard (2006).

We can split the boundary of the so-called periodic RVE into four parts (see Figure 1.5) : T (top), B (bottom), R (right) and L (left) sides. As it will be the case further in this work, we will discretize the cell using finite elements such that the nodes distribution on opposite RVE edges is equal. For every respective pair of nodes on the top-bottom and right-left boundaries we can write in the reference

[1] More information in Pierard (2006).

configuration :

$$\boldsymbol{X}_T - \boldsymbol{X}_B = \boldsymbol{X}_4 - \boldsymbol{X}_1 \tag{1.3}$$
$$\boldsymbol{X}_R - \boldsymbol{X}_L = \boldsymbol{X}_2 - \boldsymbol{X}_1 \tag{1.4}$$

where $\boldsymbol{X}_p$, p=1,2,4 are the position vectors of the vertices in the initial configuration state.

We recall the following expression :

$$\Delta\boldsymbol{x} = \boldsymbol{F} \cdot \Delta\boldsymbol{X} + \boldsymbol{w} \tag{1.5}$$

with $\Delta\boldsymbol{x}$ and $\Delta\boldsymbol{X}$ the relative position vectors with respect to an arbitrary reference point, $\boldsymbol{F}$ the macro deformation gradient tensor and $\boldsymbol{w}$ the microscopic fluctuations field.

Now consider the geometrically periodic boundary RVE on Figure 1.5. The boundary can be split in two parts : "+" and "−". Those two parts are defined by opposite outward normal vectors at the corresponding points : $\boldsymbol{n}_m^+ = \text{-}\boldsymbol{n}_m^-$. The periodic boundary conditions (PBC) can be imposed by requiring the periodicity of the microscopic fluctuations field :

$$\boldsymbol{w}^+ = \boldsymbol{w}^- \tag{1.6}$$

We apply equation 1.5 to the previous material vectors (see equations 1.3 and 1.4) connecting the reference arbitrary point (in this case, point 1 on Figure 1.5) and the corresponding ones lying on the "+" and "−" parts of the boundary. Subtraction of the obtained expression gives the formulation of the PBCs in terms of the position vectors of the boundary points :

$$\boldsymbol{x}^+ - \boldsymbol{x}^- = \boldsymbol{F} \cdot (\boldsymbol{X}^+ - \boldsymbol{X}^-) \tag{1.7}$$

It is now clear that the position vectors of the vertices nodes in the deformed configuration are prescribed following :

$$\boldsymbol{x}_p = \boldsymbol{F} \cdot \boldsymbol{X}_p \text{ with } p = 1, 2, 4 \tag{1.8}$$

where nodes p with p=1,2,4 are called "control" or "master" nodes.

We may now rewrite the PBCs from equations 1.3 and 1.4 as follows :

$$\boldsymbol{x}_T = \boldsymbol{x}_B + \boldsymbol{x}_4 - \boldsymbol{x}_1 \tag{1.9}$$
$$\boldsymbol{x}_R = \boldsymbol{x}_L + \boldsymbol{x}_2 - \boldsymbol{x}_1 \tag{1.10}$$

These conditions being both satisfied in the initial and deformed states, we can finally express those in terms of displacements :

$$\boldsymbol{u}_T = \boldsymbol{u}_B + \boldsymbol{u}_4 - \boldsymbol{u}_1 \tag{1.11}$$
$$\boldsymbol{u}_R = \boldsymbol{u}_L + \boldsymbol{u}_2 - \boldsymbol{u}_1 \tag{1.12}$$

with $\boldsymbol{u}_p = (\boldsymbol{F} - \boldsymbol{I}) \cdot \boldsymbol{X}_p$ with p=1,2,4.

Finally, we need to add and apply anti-periodicity condition of tractions :

$$\boldsymbol{t_R} = -\boldsymbol{t_L} \tag{1.13}$$

But if the periodicity of the microscopic fluctuations field is applied, the anti-periodicity of tractions is automatically satisfied (see Kouznetsova (2018)).

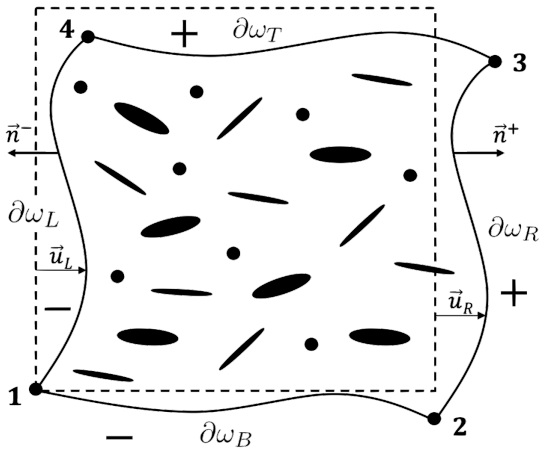

Figure 1.5: Periodic boundary conditions applied on the RVE (inspired from Pierard (2006) and Kouznetsova (2018)).

4 Micro-macro transition

Now we explain how to achieve the micro-macro transition. Suppose we carry out a classical continuum mechanics computation. From the load defined at each macroscopic point, we know the macroscopic strain $\overline{\boldsymbol{\varepsilon}}$ or stress $\overline{\boldsymbol{\sigma}}$. If we know $\overline{\boldsymbol{\varepsilon}}$ we aim at computing $\overline{\boldsymbol{\sigma}}$ and vice-versa. The goal is to compute the desired quantity using micro-mechanical models. More information about the subject can be found in the literature, e.g. Nemat-Nasser and Hori (1993) ; Aboudi (1991) or Doghri (2010).

4.1 Volume Averages

Under the load on the RVE (either an imposed macroscopically homogeneous stress or deformation field), macroscopic properties, i.e. average quantities over the whole RVE or RUC, are defined as follows :

$$\overline{\boldsymbol{f}} = \langle \boldsymbol{f}(\boldsymbol{x}) \rangle_\omega = \frac{1}{V} \int_\omega \boldsymbol{f}(\boldsymbol{x}) dV \tag{1.14}$$

where V is the volume of the RVE ω and $\boldsymbol{f}(\boldsymbol{x})$ the considered quantity field inside the RVE.

4.2 Linear displacement boundary condition

Suppose we know $\overline{\boldsymbol{\varepsilon}}$. It means that at the microscopic level the RVE is subjected to imposed displacement on its boundary $\partial\omega$:

$$\overline{u}_i(\boldsymbol{x}) = \overline{\varepsilon}_{ij} x_j(\boldsymbol{x}), \qquad \boldsymbol{x} \in \partial\omega \tag{1.15}$$

where $\overline{\varepsilon}_{ij}$ are the constant macroscopic strains.
Based on equation 1.14 we define the average strain in the RVE as follows :

$$\langle \varepsilon_{ij} \rangle_\omega \equiv \frac{1}{V} \int_\omega \varepsilon_{ij}(\boldsymbol{x}) dV \tag{1.16}$$

where $\varepsilon_{ij}(\boldsymbol{x})$, the infinitesimal strain tensor inside the RVE, is defined by :

$$\varepsilon_{ij}(\boldsymbol{x}) \equiv \frac{1}{2}\left(\frac{\partial u_i}{\partial x_j} + \frac{\partial u_j}{\partial x_i}\right) \tag{1.17}$$

Replacing equation 1.17 in equation 1.16 :

$$\langle \varepsilon_{ij} \rangle_\omega = \frac{1}{V}\int_{V_1} \frac{1}{2}\left(\frac{\partial u_i^{(1)}}{\partial x_j} + \frac{\partial u_j^{(1)}}{\partial x_i}\right) dV + \frac{1}{V}\int_{V_2} \frac{1}{2}\left(\frac{\partial u_i^{(2)}}{\partial x_j} + \frac{\partial u_j^{(2)}}{\partial x_i}\right) dV \tag{1.18}$$

where (1) and (2) respectively denote phases (1) and (2). Using the divergence theorem, the equation 1.18 becomes :

$$\langle \varepsilon_{ij} \rangle_\omega = \frac{1}{V}\int_{\partial\omega_1} \frac{1}{2}\left(u_i^{(1)} n_j + u_j^{(1)} n_i\right) dA + \frac{1}{V}\int_{\partial\omega_2} \frac{1}{2}\left(u_i^{(2)} n_j + u_j^{(2)} n_i\right) dA \tag{1.19}$$

With $\partial\omega_1$ and $\partial\omega_2$ the bounding surfaces of phases (1) and (2). Surfaces $\partial\omega_1$ and $\partial\omega_2$ contain the interface $\partial\omega_{1-2}$ and the external surface $\partial\omega$. We assume perfect contact between the two phases[2]

$$u_i^{(1)} = u_i^{(2)} \text{ on } \partial\omega_{1-2} \tag{1.20}$$

meaning that both the integrals from equation 1.19 cancel each other on the surface $\partial\omega_{1-2}$. We obtain the expression of the average strain field in a Cartesian frame as :

$$\langle \varepsilon_{ij} \rangle_\omega = \frac{1}{2V}\int_{\partial\omega} \left(u_i n_j + u_j n_i\right) dA \tag{1.21}$$

From the definition of the imposed displacement in equation 1.15, we finally have :

$$\langle \varepsilon_{ij} \rangle_\omega = \overline{\varepsilon}_{ij} \tag{1.22}$$

It means that the average strain equals the macroscopic strain, also known as the so-called *average strain theorem*.

4.3 Uniform traction boundary condition

Suppose we know $\overline{\boldsymbol{\sigma}}$. It means that at the microscopic level the RVE is subjected to imposed traction on its boundary $\partial\omega$:

$$\overline{t}_i(\boldsymbol{x}) = \overline{\sigma}_{ij} n_j(\boldsymbol{x}), \qquad \boldsymbol{x} \in \partial\omega \tag{1.23}$$

where $\boldsymbol{n}$ is the outward unit normal to $\partial\omega$. Once again, based on equation 1.14 we define the average stress[3] in the RVE as follows :

$$\langle \sigma_{ij} \rangle_\omega \equiv \frac{1}{V}\int_\omega \sigma_{ij}(\boldsymbol{x}) dV \tag{1.24}$$

[2] In the case of no perfect bonding between the two phases, the jump of displacement $[u_i] = u_i^{(2)} - u_i^{(1)}$ across $\partial\omega_{1-2}$ is not zero (see Aboudi et al. (2012)). The equ. 1.16 becomes

$$\overline{\boldsymbol{\varepsilon}} = \langle \boldsymbol{\varepsilon}(\boldsymbol{x}) \rangle_\omega = \frac{1}{V}\int_\omega \varepsilon(x) dV - \frac{1}{2V}\int_{\partial\omega_{1-2}} [u_i] n_j - [u_j] n_i dA$$

[3] Dependence of the local fields with respect to $\boldsymbol{x}$ is omitted for clarity

If we consider the equilibrium equations in absence of body forces, i.e. the RVE is self-equilibrated :

$$\nabla \cdot \boldsymbol{\sigma} = \mathbf{0}, \qquad \frac{\partial \sigma_{ij}}{\partial x_j} = 0 \tag{1.25}$$

As the gradient of $\boldsymbol{x}$ satisfies :

$$\nabla \boldsymbol{x} = \frac{\partial x_i}{\partial x_j} = \delta_{ij}$$

where δ_{ij} is Kronecker's delta, we can use this identity to express σ_{ij} as follows :

$$\sigma_{ij} = \sigma_{ik}\delta_{jk} = \sigma_{ik}\frac{\partial x_j}{\partial x_k} \tag{1.26}$$

Replacing equation 1.26 in equation 1.24, using the integration by parts and considering the self-equilibrium equation 1.25 and the B.C. (1.23) it gives :

$$\begin{aligned} \frac{1}{V}\int_\omega \sigma_{ij} dV &= \frac{1}{V}\int_{\partial\omega} \sigma_{ij} n_k x_j dA - \frac{1}{V}\int_\omega \frac{\partial \sigma_{ik}}{\partial x_k} dV \\ &= \frac{\overline{\sigma}_{ik}}{V}\int_{\partial\omega} n_k x_j dA \end{aligned} \tag{1.27}$$

Finally, as another integration by parts gives :

$$\int_{\partial\omega} x_k n_j dA = \int_\omega \frac{\partial x_k}{\partial x_j} = \delta_{kj} V$$

We have :

$$\langle \sigma_{ij} \rangle = \overline{\sigma}_{ij} \tag{1.28}$$

It means that the average stress equals the macroscopic stress, also known as the so-called *average stress theorem*.

4.4 Periodic boundary condition

In the case of periodic boundary condition, we can prove that we also get the following results :

$$\langle \varepsilon_{ij} \rangle_\omega = \overline{\varepsilon}_{ij} \tag{1.29}$$

4.5 Macroscopic response prediction

Once the boundary value problem over the RVE is solved, depending on the prescribed conditions, the macroscopic response is computed. Even if a large amount of methods are proposed to solve the problem, we will focus on the finite element method in this work. It appears from equations 1.22 and 1.28 that we can transform the problem of relating macroscopic strains and stresses $\overline{\boldsymbol{\varepsilon}}$ and $\overline{\boldsymbol{\sigma}}$ onto the problem of relating average strains and stresses $\langle \boldsymbol{\varepsilon} \rangle$ and $\langle \boldsymbol{\sigma} \rangle$. In linear elasticity, as it will be explained in section 5 of chapter 2, the problem reduces to finding the macroscopic stiffness $\overline{\boldsymbol{C}}$ such that :

$$\langle \boldsymbol{\varepsilon} \rangle = \overline{\boldsymbol{C}} : \langle \boldsymbol{\varepsilon} \rangle$$

In other words the heterogeneous micro-structure of the RVE can be replaced at the macroscopic scale with a homogeneous material of macroscopic stiffness $\overline{\boldsymbol{C}}$ (see Doghri (2000) for more details).

If prescribed uniform tractions are applied on the boundary, we get the macro strain field as macro response :

$$\overline{\boldsymbol{\varepsilon}} = \frac{1}{V}\int_{\omega} \boldsymbol{\varepsilon} dV \tag{1.30}$$

If prescribed linear displacements and periodic boundary conditions are applied on the boundary (this will be the case in what follows) we obtain a macro response in terms of stress :

$$\overline{\boldsymbol{\sigma}} = \frac{1}{V}\int_{\omega} \boldsymbol{\sigma} dV \tag{1.31}$$

This was discussed in section 4.2 and 4.4.

5 Methods to solve scale transition problem

In continuum micro-mechanics there are two main strategies for studying inhomogeneous materials. One is based on using the phase averages of the local fields and the other one on evaluating highly resolved local fields for specific micro-geometries. The latter embeds discrete models of the composite's geometry. In the ideal case they take the form of RVEs that are sufficiently large to fully describe the phase arrangement statistics. The local stress and strain fields in these models are solved by numerical engineering tools such as finite element methods, boundary element methods, and algorithms based on Fourier transforms.

FE methods

Finite element method is the most commonly used numerical method for obtaining the composite effective properties. The technique consists in meshing the RVE of the microstructure, imposing boundary conditions and solving for the stresses and strains. This method has been successfully used by many authors (see Ghossein and Lévesque (2012)) but has drawbacks. Indeed it cannot be fully automated since the meshing operation (at least) usually requires user input and computation costs can be high compared to other methods.

Full-field and mean-field homogenization

Mean-field models typically give rise to analytical or semi-analytical procedures and, as a consequence, enjoy low computational requirements compared to other methods. As a consequence to this it requires less in terms of computation costs than unit cell. Most mean-field models are based on Eshelby's solution for single ellipsoidal inclusions in an infinite matrix (Eshelby and Peierls (1957)).

In the present work we only use full-field finite element (FE) versions of the methods we considered. A large range of other methods exists (methods using Fast Fourier Transforms (FFT, ...) but they are not subject of this work (see Duschlbauer et al. (2006) for more information).

Chapter 2

Full-field finite element homogenization

1 Elastic Material Properties

In this work, the elastic properties used for the material components of the composite are similar to short glass fiber reinforced thermoplastic polymers.
The same elastic properties of composite constituents were prescribed for all performed analyses; these for the matrix :

$$E_m = 3100 \text{ [MPa]}; \quad \nu_m = 0.35$$

and these used for the fibers (with an aspect ratio $A_r = 24$) :

$$E_f = 76000 \text{ [MPa]}; \quad \nu_f = 0.22$$

2 2D cells

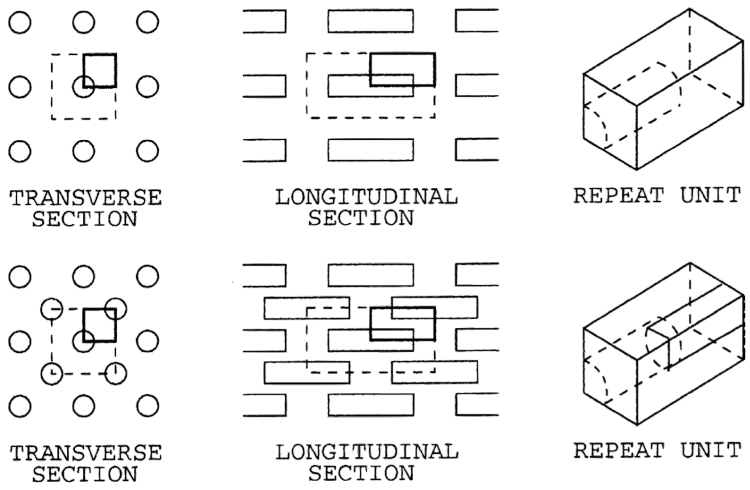

Figure 2.1: Aligned fibers and staggered fiber arrangements (from Doghri and Friebel (2005)).

In this section we will discuss the characterization of the 2D unit cell used to run the simulations and compute the macroscopic response of the composite, using periodic boundary conditions introduced previously.

First of all we define the so-called 2D unit cell dimension using the volume fractions of the fibers and matrix, respectively v_f and v_m, within the composite :

$$v_f = \frac{2ld}{LD} \; ; \quad v_m = 1 - v_f \tag{2.1}$$

with l and d respectively the length and width of the fibers, L and D respectively those ones of the cell (see Figure 2.2).

We compute the length of the fibers l using the aspect ratio $A_r = \frac{l}{d}$, with a fixed width value. It remains one equation left in order to compute the dimensions of the unit cell for a fixed v_f; this equation is proposed after Kang and Gao (2002), assuming that :

$$L - D = l - d \tag{2.2}$$

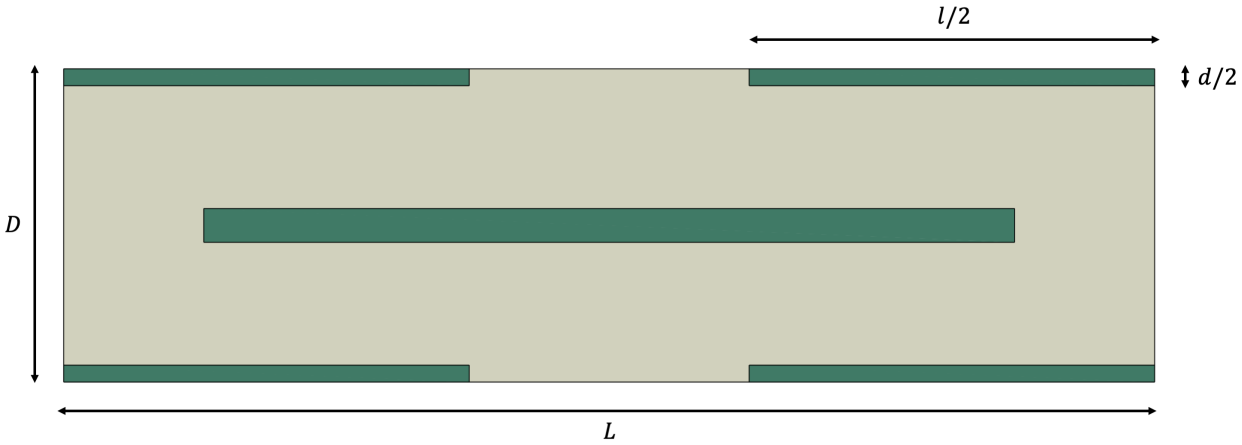

Figure 2.2: 2D unit cell with a matrix and fibers phases ($v_f = 16\%$). Dark green : fibers phase. Light green : matrix phase.

Before adding some porosity, which is the main subject of this work, we will compute and check if the results are correct when compared to those obtained for an RVE, in the case of a two-phase composite composed of a matrix and fibers phase. This will be tested on the 2D unit cell presented on Figure 2.2 using fiber volume fractions of 10%, 16%, 23% and 30% (see table 2.1 for dimensions of the unit cell in function of parameter v_f).

In a second time, we will add cavities to generate some porosity inside the composite. The cavities inside the 2D unit cell are modeled by simple cylinders (in 2D) or spheres (in 3D). The diameter of the cavities is determined by a convergence study when after three random cavities placement inside the cell results seem more or less converged.

2.1 Generation of random microstructure

To generate the unit cell, we introduce some parameters to place each cavity individually within the cell : the minimum distance between the cavity itself and the boundary of the matrix and fibers edges and finally the minimum distance between two cavities (in order to prevent them from overlapping).

A wide range of microstructures in the literature are generated using the Random Sequential Adsorption (RSA) algorithm (Rintoul and Torquato (1997)). Following this algorithm, the position of the first cavity is randomly generated. The position of a second cavity is subsequently drawn. If both cavities are in contact or overlap, the second one is redrawn until it does not collide the first. This process is repeated until the desired volume fraction and number of cavities are reached.
It turns out that this algorithm does not allow to reach high volume fraction ($> 30\%$). A short review by Ghossein and Lévesque (2012) gives some examples of authors who developed improved version of the RSA algorithm but at a higher computational cost. From the same latter review we learn that Lubachevsky and Stillinger (1990) came up with an alternative algorithm based on molecular dynamics and applied it for disk and sphere (Lubachevsky et al. (1991)). This algorithm goes as follows : all the required particles are initially created but have no volume. The particles are put in motion with their radius increasing throughout the computation. They will collide with each other or with the faces of the cell. Once the desired volume fraction of particles is reached, the simulation ends. This algorithm, although more complex than the RSA, can reach higher volume fraction, up to the theoretical dense packing, while requiring low computational cost. See Ghossein and Lévesque (2012) for more information and complete description of the latter algorithm.

In this work, as the highest volume fraction of the cavities is 10% the material will not be that dense, this is why we will follow an algorithm close to RSA procedure, using a normal distribution to generate random position of the cavities within the cell. This results in the 2D unit cell presented on Figure 2.3.

Note that a minimum fiber/voids spacing is enforced to ensure the presence of a matrix layer between neighboring fibers (and avoiding overlapping).

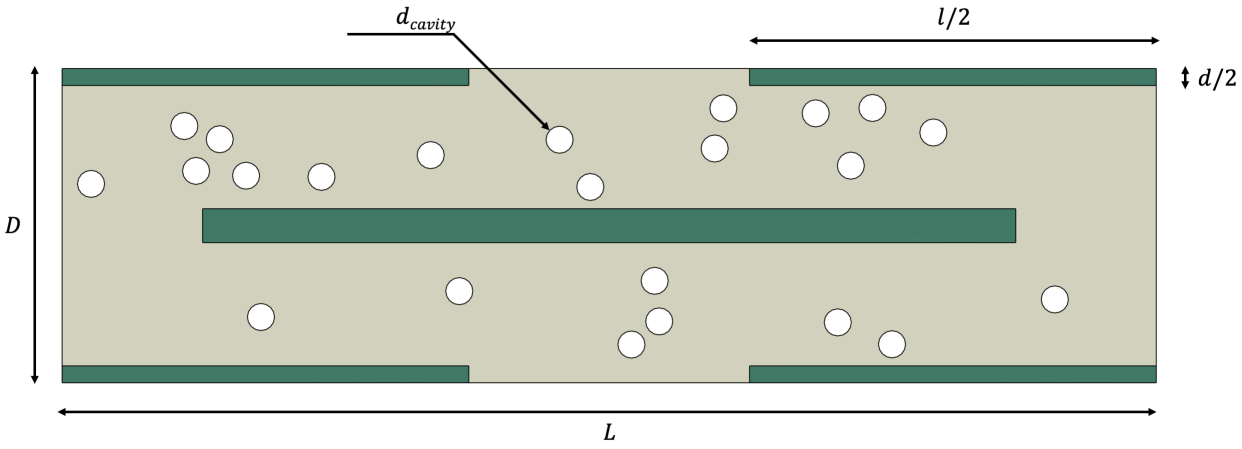

Figure 2.3: 2D unit cell with a matrix and fibers phases ($v_f = 16\%$) with some porosity ($v_p = 4\%$). Dark green : fibers phase. Light green : matrix phase.

v_f	d	l	L	D
10	1	24	36.2437	13.2437
16	1	24	32.2906	9.2906
23	1	24	29.9647	6.9647
30	1	24	28.5953	5.5953

Table 2.1: Dimensions of the unit cell in function of the fibers' volume fraction.

3 Periodic Boundary Conditions implementation in Abaqus

We introduced PBC in the previous chapter. Periodic boundary conditions are prescribed to ensure compatible deformation modes for any load state of the unit cell. Applying PBC in FEA software like Abaqus (2019) implies to express relations 1.11 and 1.12 in a discretized format. It leads to a set of homogeneous constraints of the type :

$$\boldsymbol{A}\ \boldsymbol{u} = 0 \tag{2.3}$$

with $\boldsymbol{A}$ the matrix containing constraint coefficients and $\boldsymbol{u}$ a column vector containing the degrees of freedom involved by the constraints.

As recalled in Wu et al. (2014), constraint equations in Abaqus (2019) are defined by :

$$A_1 u_i^p + A_2 u_j^q + ... + A_N u_k^R = 0 \tag{2.4}$$

with R a node, k the d.o.f. and A_N a constant imposing the constraint.

Instead of applying PBC directly on each pair of homologous nodes, we can use the so-called "dummy" node Z. Indeed we can apply all the PBCs of the homologous pairs of nodes through this dummy node using equation 2.4 by replacing the zero of the right-hand side (RHS) by a non-zero value $\hat{u}$:

$$A_1 u_i^p + A_2 u_j^q + ... + A_N u_k^R = \hat{u} \tag{2.5}$$

with $\hat{u}$ the prescribed value such as a strain or displacement.

Note that the dummy node Z is not attached to any other part in the model. Though this node will not be connected to any part in the model, we define a reference point with arbitrary coordinates to represent it. So we specify boundary condition with a value $\hat{u}$ in a certain direction directly on this reference point itself.

Once the dummy node is created, we have to link the homologous nodes in some way. To do so two sets of nodes are created. Consider a unit cell defined as in Figure 2.2. One of those node sets contains nodes that belong to one of two pairs of opposed faces (i.e. bottom/left sides or top/right sides) and the other set contains nodes of the respective opposed face. To summarize we will apply periodic boundary conditions of opposed pairs of boundary sides linked to a dummy node through the equation constraint in Abaqus (2019).

To be sure we correctly link a pair of homologous nodes, we have to ensure that the mesh is structured, at least along the boundary of the discretized model. It means that the mesh is enforced to be identical on opposite faces of the cell, so that the nodes can be paired off and their corresponding degrees of freedom linked via linear constraint equations.

Homtools

The procedure described here above is not especially a straightforward task. This is why we used instead a plugin to Abaqus (2019) called *Homtools* (Lejeunes and Bourgeois (2011)). This plugin enables to interact directly from the CAE window. To correctly use it we define two reference points : one to link the two opposed bottom/top sides of the unit cell and other one to link the left/right sides.

If the mechanical macro loading we want to carry out is a traction test, the load will be applied on the first reference point (RP-1 in Figure 2.5), if it is a shear test the load will be applied on the second

reference point (RP-2). On Figure 2.5 the boundary sets stand for the pairs of opposed sides while the periodicity vector represent the distance between those pairs of boundary sides. We will use this plugin two times : one for the bottom/top boundaries and an other one for the left/right ones. After the tying relations are applied on paired nodes, the model looks like Figure 2.4 where we can see the pairing applied all along the boundary.

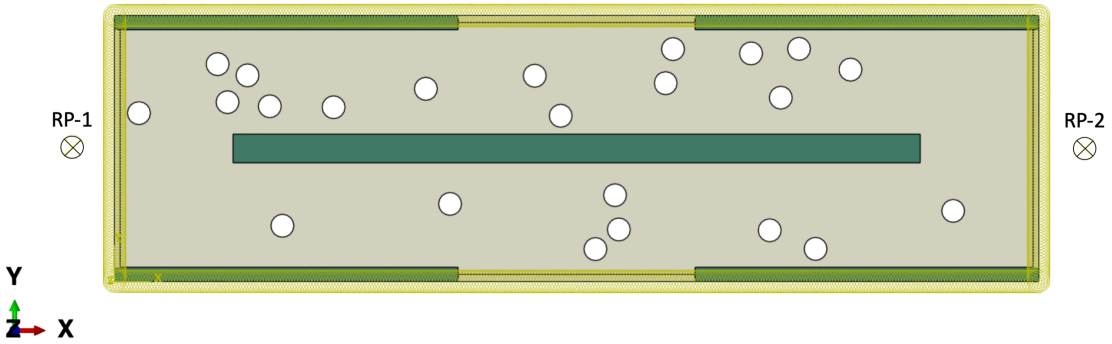

Figure 2.4: Pairing of homologous nodes on opposed boundary sides using Homtools plugin. Reference points are denoted RP-1 and RP-2.

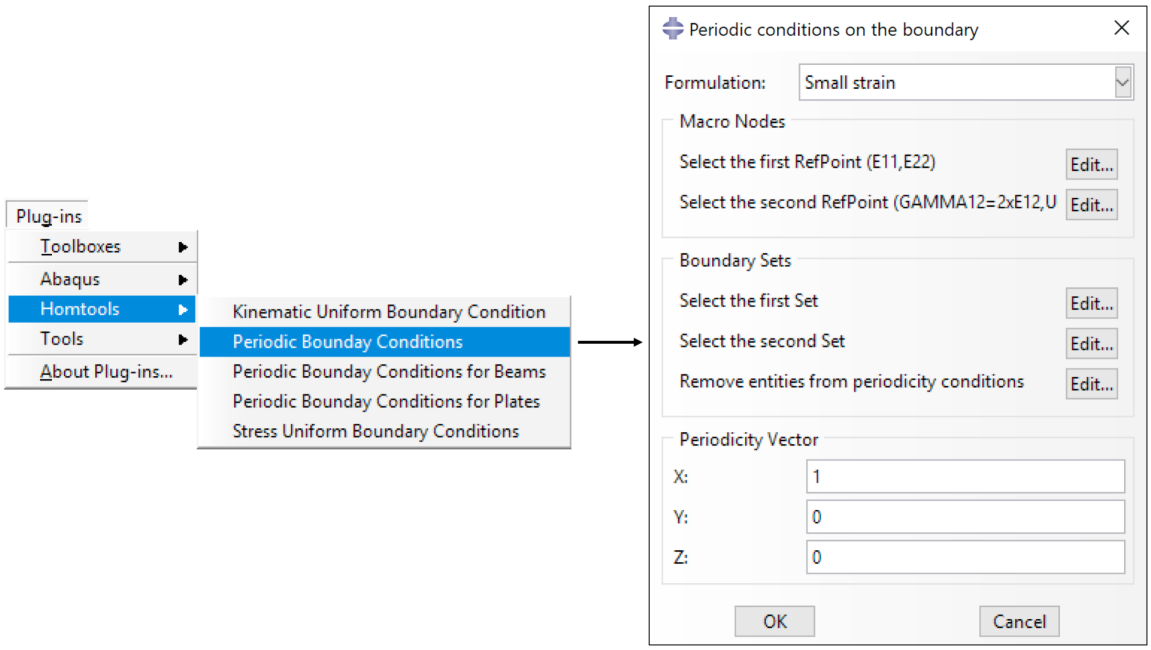

Figure 2.5: PBC definition using Homtools plugin

4 Finite Element Meshing

The microstructure of the unit cell is meshed using mixing of structured and free meshing techniques. On the one hand the former guarantees an even distribution of the nodes along the boundaries of the cell, to be sure there are for each one of them pairs of homologous nodes all along and then apply periodic boundary conditions. On the other hand utilization of free mesh elements will allow to respect the shape of the inclusions within the cell, even if they are modeled by simple 2D cylinders with

regular edges.

On Figure 2.6 there is an example of typical meshing of the UD unit cell used to compute the overall properties of the composite. In this particular case, a number of 35828 elements have been used : 34892 are linear quadrilateral elements of type CPS4R and 936 linear triangular elements of type CPS3 (because in this particular case, plane stress is assumed).

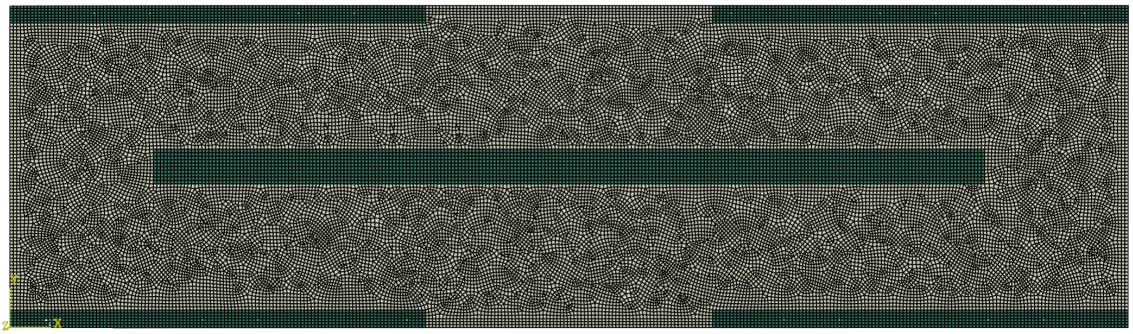

Figure 2.6: Mixing meshing of the UD unit cell ($v_p = 16\%$) : structured plane stress elements with free plane stress elements (35828 elements with an approximate element size of $h = 0.1$).

5 Generalized Hooke's law (constitutive equations)

To meaningfully assess the composite material durability, strength etc. we need to estimate the stresses and strains occurring within the loaded composite structure. A wide range of constitutive materials providing the mathematical link between stress and strain have been proposed and utilized, each of them with its own limitations. This work is limited to linear elasticity, thus using Hooke's model :

$$\boldsymbol{\sigma} = \boldsymbol{C} : \boldsymbol{\varepsilon}, \text{ i.e. } \sigma_{ij} = C_{ijkl}\varepsilon_{kl} \tag{2.6}$$

where σ_{ij} and ε_{ij} are respectively the stress and strain components and C_{ijkl} the fourth-order elastic stiffness tensor components. The relationship between stress and strain is fully reversible. It means that when loaded the material deforms and recovers completely once unloaded.
Due to symmetries, the elastic tensor $\mathbf{C}$ can be represented by 21 independent scalar components, allowing to represent it with a 6×6 symmetric matrix : the stiffness matrix.

Considering only the in-plane components (as we are in 2D) of the stiffness matrix and using the Voigt notation, it gives for an anisotropic material :

$$\begin{pmatrix} \sigma_{11} \\ \sigma_{22} \\ \sigma_{12} \end{pmatrix} = \begin{pmatrix} C_{11} & C_{12} & C_{16} \\ C_{12} & C_{22} & C_{26} \\ C_{16} & C_{62} & C_{66} \end{pmatrix} \begin{pmatrix} \varepsilon_{11} \\ \varepsilon_{22} \\ 2\varepsilon_{12} \end{pmatrix} \tag{2.7}$$

This relation can be inverted to express the strain components as function of the stress components. The inverse of the stiffness matrix is known as the compliance matrix. It reads :

$$\begin{pmatrix} \varepsilon_{11} \\ \varepsilon_{22} \\ 2\varepsilon_{12} \end{pmatrix} = \begin{pmatrix} S_{11} & S_{12} & S_{16} \\ S_{12} & S_{22} & S_{26} \\ S_{16} & S_{62} & S_{66} \end{pmatrix} \begin{pmatrix} \sigma_{11} \\ \sigma_{22} \\ \sigma_{12} \end{pmatrix} \tag{2.8}$$

Due to symmetries depending on the studied case, the stiffness and compliance matrices may degenerate into simpler cases where the number of independent components needed to described the material linear elastic behavior is reduced. Two particular cases will be encountered in what follows : orthotropic materials and transversely isotropic materials. We will now briefly focus on those particular cases.

5.1 Orthotropic materials

By definition, orthotropic materials present three orthogonal symmetry planes. It implies that both $[\boldsymbol{C}]$ and $[\boldsymbol{S}]$ matrices are invariant under the three following transformations (3D case) :

$$[P_1] = \begin{pmatrix} -1 & 0 & 0 \\ 0 & 1 & 0 \\ 0 & 0 & 1 \end{pmatrix} ; [P_2] = \begin{pmatrix} 1 & 0 & 0 \\ 0 & -1 & 0 \\ 0 & 0 & 1 \end{pmatrix} ; [P_3] = \begin{pmatrix} 1 & 0 & 0 \\ 0 & 1 & 0 \\ 0 & 0 & -1 \end{pmatrix} \tag{2.9}$$

with $[P_i]$, i=1,2,3 the transformation matrices.

This reduces the number of independent parameters of such stiffness (compliance) matrix to nine in 3D, and in 2D, only four in-plane properties are needed :

$$\begin{pmatrix} \sigma_{11} \\ \sigma_{22} \\ \sigma_{12} \end{pmatrix} = \begin{pmatrix} C_{11} & C_{12} & 0 \\ C_{12} & C_{22} & 0 \\ 0 & 0 & C_{66} \end{pmatrix} \begin{pmatrix} \varepsilon_{11} \\ \varepsilon_{22} \\ 2\varepsilon_{12} \end{pmatrix} \tag{2.10}$$

5.2 Transversely isotropic materials

By definition transversely isotropic materials present uniform material properties in one plane (for instance, (1,2)-plane). This is a particular case of orthotropic materials where the properties are different in the normal direction to this plane (in this case, direction 3). The number of independent parameters required to describe this type of material reduces to five in 3D. In the (1,2) plane of isotropy, there are two independent constants (C_{11}=C_{22} and C_{12} in equation 2.10).
Compute the stiffness and compliance matrices will allow to estimate the engineering constants describing the material.

6 Homogenization of elastic composites

6.1 Effective elasticity tensors and engineering constants

Based on the previous section, we are now able to compute the engineering constants. Using effective stress and strain components $\overline{\sigma}_{ij}$ and $\overline{\varepsilon}_{ij}$ described on section 4.5 , respectively, we can derive the effective stiffness matrix $[\overline{\boldsymbol{C}}]$:

$$\overline{\boldsymbol{\sigma}} = \overline{\boldsymbol{C}} : \overline{\boldsymbol{\varepsilon}} \tag{2.11}$$

where the operator ":" stands for the double contracted product.
So for any orthotropic material, we get the expression of the effective stiffness matrix :

$$\begin{pmatrix} \overline{\sigma}_{11} \\ \overline{\sigma}_{22} \\ \overline{\sigma}_{12} \end{pmatrix} = \begin{pmatrix} \overline{C}_{11} & \overline{C}_{12} & 0 \\ \overline{C}_{12} & \overline{C}_{22} & 0 \\ 0 & 0 & \overline{C}_{66} \end{pmatrix} \begin{pmatrix} \overline{\varepsilon}_{11} \\ \overline{\varepsilon}_{22} \\ 2\overline{\varepsilon}_{12} \end{pmatrix} \tag{2.12}$$

of which the inverse gives the effective compliance matrix :

$$\begin{pmatrix} \overline{\varepsilon}_{11} \\ \overline{\varepsilon}_{22} \\ 2\overline{\varepsilon}_{12} \end{pmatrix} = \begin{pmatrix} \overline{S}_{11} & \overline{S}_{12} & 0 \\ \overline{S}_{12} & \overline{S}_{22} & 0 \\ 0 & 0 & \overline{S}_{66} \end{pmatrix} \begin{pmatrix} \overline{\sigma}_{11} \\ \overline{\sigma}_{22} \\ \overline{\sigma}_{12} \end{pmatrix} \tag{2.13}$$

In 2D considerations three independent load cases are required for a complete description of the mechanical response of the composite : either simple tension tests in direction 1 and 2 or a shear test in (1,2) plane. For instance, for a tension test in direction 1 the unit cell is subjected to a corresponding macro strain $\overline{\boldsymbol{\varepsilon}}$:

$$\overline{\boldsymbol{\varepsilon}} = \begin{pmatrix} 0.1 \\ 0 \\ 0 \end{pmatrix} \tag{2.14}$$

We will carry out two types of analyses, each one of them implying a different assumption : plane stress and plane strain.

Plane stress

Plane stress assumes an infinitely thin solid where the out-of-plane dimension is much smaller compared to the in-plane dimensions, meaning that $\sigma_{33} = 0$ (but $\varepsilon_{33} \neq 0$). We will impose periodic boundary conditions on the unit cell in order to only have a non-zero stress component in the direction of the carried test. We can summarize the strain components (without loss of generality) :

$$\overline{\varepsilon}_{11} \neq 0,\ \overline{\varepsilon}_{22} \neq 0,\ \overline{\varepsilon}_{12} \neq 0$$

and strain components the following way, depending on the test :

- Traction test in direction 1 : $\overline{\sigma}_{11} \neq 0$, $\overline{\sigma}_{22} = 0$, $\overline{\sigma}_{12} = 0$
- Traction test in direction 2 : $\overline{\sigma}_{11} = 0$, $\overline{\sigma}_{22} \neq 0$, $\overline{\sigma}_{12} = 0$
- Shear test : $\overline{\sigma}_{11} = 0$, $\overline{\sigma}_{22} = 0$, $\overline{\sigma}_{12} \neq 0$

To compute all engineering constants of the composite in plane strain we will compute the full compliance tensor. Indeed using definition of the effective compliance matrix equation 2.13, we read the following components.

Consider a traction test in direction 1 :

$$\overline{\varepsilon}_{11} = \overline{S}_{11}\overline{\sigma}_{11} \rightarrow \overline{S}_{11} = \frac{\overline{\varepsilon}_{11}}{\overline{\sigma}_{11}} \equiv \frac{1}{\overline{E}_1} \tag{2.15}$$

$$\overline{\varepsilon}_{22} = \overline{S}_{12}\overline{\sigma}_{11} \rightarrow \overline{S}_{12} = \frac{\overline{\varepsilon}_{22}}{\overline{\sigma}_{11}} = \frac{\overline{\varepsilon}_{22}}{\overline{\varepsilon}_{11}}\frac{\overline{\varepsilon}_{11}}{\overline{\sigma}_{11}} \equiv \frac{-\overline{\nu}_{12}}{\overline{E}_1} \tag{2.16}$$

with $\overline{E}_1$ and $\overline{\nu}_{12}$ the effective Young's modulus in direction 1 and Poisson's coefficient, respectively.

Consider now a traction test in direction 2 :

$$\overline{\varepsilon}_{11} = \overline{S}_{12}\overline{\sigma}_{22} \rightarrow \overline{S}_{12} = \frac{\overline{\varepsilon}_{11}}{\overline{\sigma}_{22}} = \frac{\overline{\varepsilon}_{11}}{\overline{\varepsilon}_{22}}\frac{\overline{\varepsilon}_{22}}{\overline{\sigma}_{22}} \equiv \frac{-\overline{\nu}_{21}}{\overline{E}_2} \tag{2.17}$$

$$\overline{\varepsilon}_{22} = \overline{S}_{22}\overline{\sigma}_{22} \rightarrow \overline{S}_{22} = \frac{\overline{\varepsilon}_{22}}{\overline{\sigma}_{22}} \equiv \frac{1}{\overline{E}_2} \tag{2.18}$$

with $\overline{E}_2$ and $\overline{\nu}_{21}$ the effective Young's modulus in direction 2 and Poisson's coefficient, respectively.

Finally consider shear test in direction (1,2) :

$$2\overline{\varepsilon}_{12} = \overline{S}_{66}\overline{\sigma}_{12} \rightarrow \overline{S}_{66} = 2\frac{\overline{\varepsilon}_{12}}{\overline{\sigma}_{12}} \equiv \frac{1}{\overline{G}_{12}} \tag{2.19}$$

with $\overline{G}_{12}$ the effective shear modulus.

Note that for symmetry reasons, there is the following equivalence

$$\frac{\overline{\nu}_{ij}}{\overline{E}_i} = \frac{\overline{\nu}_{ji}}{\overline{E}_j} \text{ (no summation)} \tag{2.20}$$

even though $\overline{\nu}_{ij} \neq \overline{\nu}_{ji}$ and $\overline{E}_i \neq \overline{E}_j$ in general.

All the effective engineering constants are now known : $\overline{E}_1$, $\overline{E}_2$, $\overline{\nu}_{12}$, $\overline{\nu}_{21}$ and $\overline{G}_{12}$.

Plane strain

Plane strain assumes an infinitely long solid where the out-of-plane dimension is much larger compared to the in-plane dimensions, meaning that $\varepsilon_{33} = 0$ (but $\sigma_{33} \neq 0$). In this case we will impose periodic boundary conditions on the unit cell in order to only have a non-zero strain component in the direction of the carried test. We can summarize the stress components (without loss of generality) :

$$\overline{\sigma}_{11} \neq 0,\ \overline{\sigma}_{22} \neq 0,\ \overline{\sigma}_{12} \neq 0$$

and strain components the following way, depending on the test :

- Traction test in direction 1 : $\overline{\varepsilon}_{11} \neq 0$, $\overline{\varepsilon}_{22} = 0$, $\overline{\varepsilon}_{12} = 0$
- Traction test in direction 2 : $\overline{\varepsilon}_{11} = 0$, $\overline{\varepsilon}_{22} \neq 0$, $\overline{\varepsilon}_{12} = 0$
- Shear test : $\varepsilon_{11} = 0$, $\overline{\varepsilon}_{22} = 0$, $\overline{\varepsilon}_{12} \neq 0$

To compute all engineering constants of the composite in plane strain we will first compute the full stiffness tensor in the same way as it was explained for the compliance matrix in plane stress (equations 2.15 to 2.19). Then we simply invert the stiffness matrix in order to get the compliance matrix and so the desired effective engineering constants based on their definition in those same equations.

All the effective engineering constants are now known : $\overline{E}_1$, $\overline{E}_2$, $\overline{\nu}_{12}$, $\overline{\nu}_{21}$ and $\overline{G}_{12}$. However, note that these engineering constant cannot be interpreted in the same way as under plane stress consideration due to the non-zero out-of-plane stress σ_{33}. It means that when we will carry out a tensile test in direction 1 or 2 we won't be able to have only one non-zero constrain component. Plane stress assumption on the contrary gives the real engineering constants, i.e. following the classical definition of those constants. Note that we can go from plane strain problem to plane stress problem and vice-versa using substitutions relations (see Doghri (000b) for more details).

Example of mechanical tests using PBCs

On figures 2.7a to 2.7c we can see contour plots of the Von Mises stress field in a UD unit cell subjected to several mechanical loadings using PBCs and assuming plane stress state. The study case is a basic UD unit cell composed of an homogeneous matrix and fibers reinforcement of $v_p = 16\%$. The mesh is the same we presented on Figure 2.6 in chapter 2.

6.2 Mean-field homogenization

The strain averages per phase are related through a (still unknown) strain concentration tensor $\boldsymbol{B}^{\varepsilon}$:

$$\langle \boldsymbol{\varepsilon} \rangle_{\omega_1} = \boldsymbol{B}^{\varepsilon} : \langle \boldsymbol{\varepsilon} \rangle_{\omega_0} \tag{2.21}$$

$$\langle \boldsymbol{\varepsilon} \rangle_{\omega_1} = \boldsymbol{A}^{\varepsilon} : \overline{\boldsymbol{\varepsilon}} \tag{2.22}$$

with

$$\boldsymbol{A}^{\varepsilon} = \boldsymbol{B}^{\varepsilon} : (v_1 \boldsymbol{B}^{\varepsilon} + v_0 \boldsymbol{I})^{-1}$$

where $\boldsymbol{I}$ stands for the fourth-order symmetric identity tensor. For any homogenization model defined by $\boldsymbol{B}^{\varepsilon}$, we can prove (see Doghri (2018)) that the macro stiffness is given by :

$$\overline{\boldsymbol{C}} = [v_1 \boldsymbol{C}_1 : \boldsymbol{B}^{\varepsilon} + (1 - v_1)\boldsymbol{C}_0] : [v_1 \boldsymbol{B}^{\varepsilon} + (1 - v_1)\boldsymbol{I}]^{-1} \tag{2.23}$$

Further away we will use some well-known homogenization schemes that we briefly recall here below as introduction of what will follow next. Classically we could use mean-field methods based on analytical model. Voigt, Reuss and Mori-Tanaka models are well-known models. They are defined as follows :

Voigt model

This scheme assumes uniform strain inside the RVE, it results :

$$\boldsymbol{B}^{\varepsilon} = \boldsymbol{I}$$

$$\overline{\boldsymbol{C}} = v_1 \boldsymbol{C}_1 + (1 - v_1)\boldsymbol{C}_0$$

Reuss model

This scheme assumes uniform stress inside the RVE, it results :

$$\boldsymbol{B}^{\varepsilon} = \boldsymbol{C}_1^{-1} : \boldsymbol{C}_0$$

$$\overline{\boldsymbol{C}} = [v_1 \boldsymbol{C}_1^{-1} + (1 - v_1)\boldsymbol{C}_0^{-1}]^{-1}$$

Voigt and Reuss models are known to give respectively upper and lower bounds for $\overline{\boldsymbol{C}}$, but none of them take into account neither the shape nor the orientation of the inclusions. Their interest regarding multi-phase composite materials is then quite not really helpful, except when there are used in the second step of the homogenization for multi-phase composites (see chapter 4).

Mori-Tanaka (MT)

This scheme ends with a strain concentration tensor equal to the one of the single-inclusion problem :

$$\boldsymbol{B}^{\varepsilon} = \boldsymbol{H}^{\varepsilon}(I, \boldsymbol{C}_0, \boldsymbol{C}_1)$$

with $\boldsymbol{H}$ the Eshelby's tensor. For this reason Benveniste (1987) came up with the following interpretation of MT : "each inclusion (I) behaves like an isolated inclusion in the matrix seeing $\langle \boldsymbol{\varepsilon} \rangle_{\omega_0}$ as a far-field strain".

However, in this work, rather than using analytical or semi-analytical model for Mori-Tanaka, we will use full-field models inspired by Mori-Tanaka.

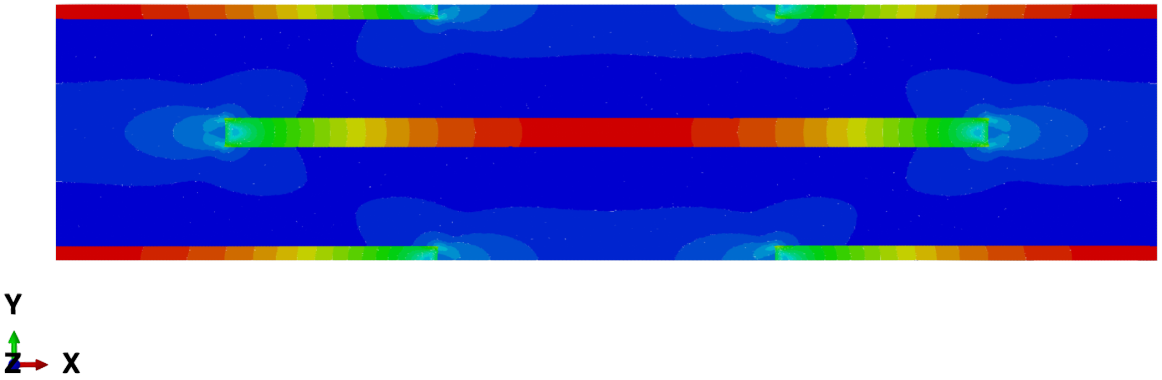

(a) Tension test in direction 1, i.e. direction of the fibers.

(b) Tension test in direction 2, i.e. transverse direction.

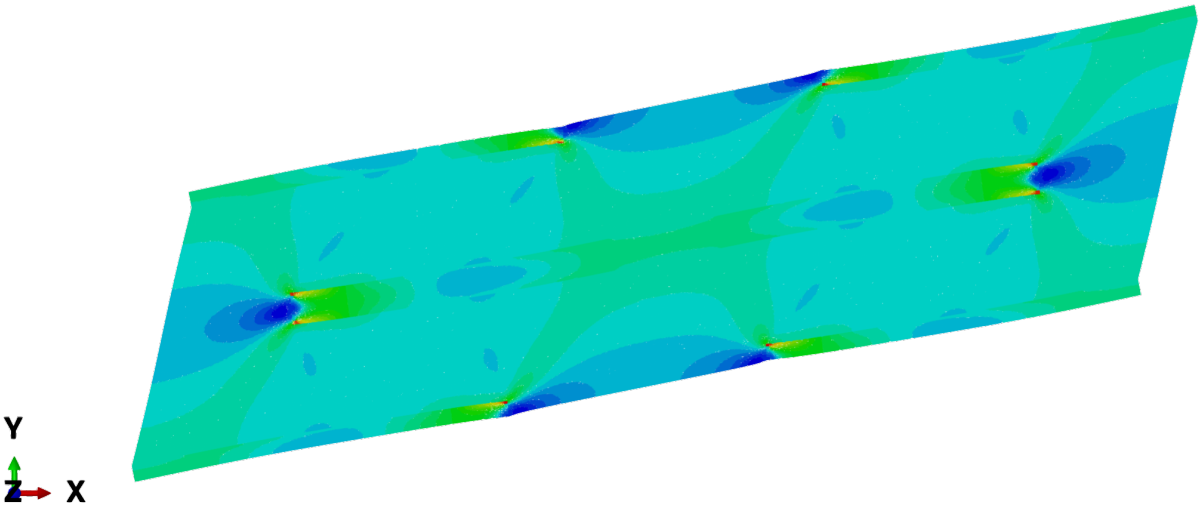

(c) Shear test.

Figure 2.7: Typical equivalent Von Mises stress contour plots resulting from tension and shear tests in the case of $v_p = 16\%$ on the deformed configuration. The warmer the colors, the more important the stress. The colder the colors, the lower the stress.

7 Macroscopic stress and strain computation (Abaqus)

Once the analysis of the microscopic unit cell is completed, we can extract average stress and strain. We already derived the volume integral in equation 1.31 in chapter 1 to compute the macro stress response. We could use this relation but there is a computationally more efficient way to post-process the macro stress response by means of a surface integral instead of a volume integral, which becomes even more simple due to the periodic boundary conditions. The latter surface integral may be express as follows (see Kouznetsova (2018)) :

$$\overline{\boldsymbol{\sigma}} = \frac{1}{V}\int_{\partial\omega} \boldsymbol{t}\mathbf{x}dA \tag{2.24}$$

with $\boldsymbol{t}$ the traction vector.

Now consider all forces acting on the unit cell boundary subjected to PBC introduced in chapter 1 :

$$\mathbf{u}_p = (\boldsymbol{F} - \boldsymbol{I}) \cdot \mathbf{x}_p$$

with $p = 1, 2, 4$.

We recall :

$$\mathbf{x}_p = \mathbf{F} \cdot \mathbf{X}_p, \ p = 1, 2, 4 \tag{2.25}$$

and

$$\mathbf{x}_T = \mathbf{x}_B + \mathbf{x}_4 - \mathbf{x}_1 \tag{2.26}$$
$$\mathbf{x}_R = \mathbf{x}_L + \mathbf{x}_2 - \mathbf{x}_1 \tag{2.27}$$

Resulting external forces $\mathbf{f}_p^{ext}$ act at the three prescribed corner nodes $p = 1, 2, 4$. Additionally to these forces are forces involved in every constraint (or so-called tying) relation we recall here above. On Figure 2.8, tying forces are denominated $\mathbf{p}^{t1}$.
For instance :

- From top-bottom : $\mathbf{p}_B^t$, $\mathbf{p}_T^t$, $\mathbf{p}_1^{t_B}$ and $\mathbf{p}_4^{t_B}$
- From left-right : $\mathbf{p}_L^t$, $\mathbf{p}_R^t$, $\mathbf{p}_1^{t_L}$ and $\mathbf{p}_2^{t_L}$

Following Kouznestova notes, only the external forces at the prescribed corner nodes contribute to the macroscopic stress. This is mainly due, among other reasons, to the periodicity of homologous nodes that induce anti-periodicity of tractions on the opposite boundaries, i.e.

$$\mathbf{p}_B^t = -\mathbf{p}_T^t$$
$$\mathbf{p}_L^t = -\mathbf{p}_R^t$$

For instance, for each constraint relation between pairs of nodes on the bottom-top boundaries there are a tying force at the node on the bottom boundary $\mathbf{p}_B^t$, a tying force at the node on the top boundary $\mathbf{p}_T^t$ and tying forces at the corner nodes 1 and 4, $\mathbf{p}_1^{t_B}$, $\mathbf{p}_4^{t_B}$, respectively. And similarly there are forces $\mathbf{p}_L^t$, $\mathbf{p}_R^t$, $\mathbf{p}_1^{t_L}$ and $\mathbf{p}_2^{t_L}$ corresponding to the left-right constraints. All those forces are schematically shown on figure 2.8.

[1] For the sake of simplicity and understanding we will use from now on the notation used by Kouznetsova in her notes and schematic pictures.

Based on the condition of zero virtual work and using the periodic boundary conditions and the relation between the tying forces relations, it is proven (Kouznetsova (2018)) that :

$$\overline{\sigma} = \frac{1}{V} \sum_{p=1,2,4} \mathbf{f}_p^{ext} \mathbf{x}_p \tag{2.28}$$

where nodes p are the master nodes introduced in chapter 1. It means that average stress computation using periodic boundary conditions only requires the reaction forces at each master node. Note that we may have used the average stress definition given by equation 1.24 in chapter 1 but equation 2.28 is much more computationally-friendly as it does not require to recover local stress over the whole elements of the mesh.

We could use the average strain over all the elements of the mesh but we won't, for two reasons : firstly it will generate high computational costs when using finer meshes and secondly Abaqus (2019) does not provide strain inside the cavities. For that reason and because we know we can prove that for periodic boundary conditions, we get $\langle \boldsymbol{\varepsilon} \rangle_\omega = \overline{\boldsymbol{\varepsilon}}$, using the definition of the infinitesimal strain tensor and considering master nodes of Figure 2.8 we end up with these simple following equations :

$$\overline{\varepsilon}_{11} = \frac{u_1(\mathbf{2}) - u_1(\mathbf{1})}{x_1(\mathbf{2}) - x_1(\mathbf{1})} \tag{2.29}$$

$$\overline{\varepsilon}_{22} = \frac{u_2(\mathbf{4}) - u_2(\mathbf{1})}{x_2(\mathbf{4}) - x_2(\mathbf{1})} \tag{2.30}$$

$$\overline{\varepsilon}_{12} = \frac{1}{2} \left(\frac{u_2(\mathbf{2}) - u_2(\mathbf{1})}{x_1(\mathbf{2}) - x_1(\mathbf{1})} + \frac{u_1(\mathbf{4}) - u_1(\mathbf{1})}{x_2(\mathbf{4}) - x_2(\mathbf{1})} \right) \tag{2.31}$$

where $\boldsymbol{i} = \mathbf{1}, \mathbf{2}, \mathbf{4}$ denotes master nodes of Figure 2.8.

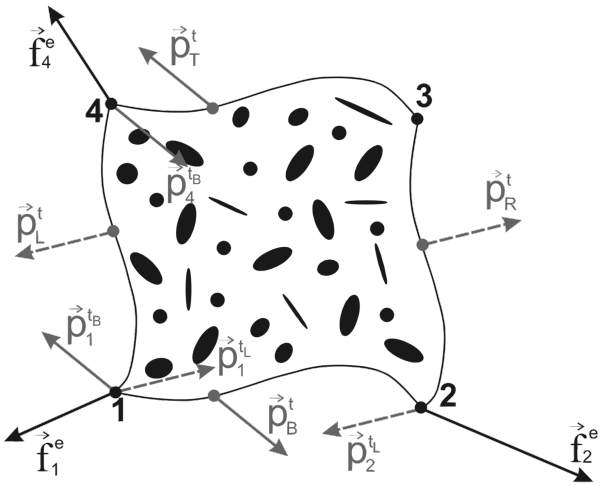

Figure 2.8: Schematic picture of the tying forces acting on the boundary of a 2D RVE subjected to PBC. From Kouznetsova (2018).

Chapter 3

Porous composites with aligned short fibers reinforcement

1 Model description

In this section we will study and compare two homogenization procedures to compute the overall mechanical properties of the composite : firstly with direct FEA and secondly following a decomposition of the homogenization procedure into two levels (deep and high levels respectively). The microstructure is composed of aligned short fibers and cavities embedded in the matrix.

1.1 Direct full-field homogenization

Using finite element method, we carry out the loading tests directly on the material composed by a matrix with some porosity and inclusions we modeled by the 2D unit cell we depicted on figure 2.3.

1.2 Two-level homogenization

In the two-level homogenization method (see figure 3.1) we consider a deep level composed of two phases : the matrix with some cavities. The high level is a two-phase material composed of short fibers embedded in the homogenized matrix from the deep level. Both levels are homogenized by FEA.

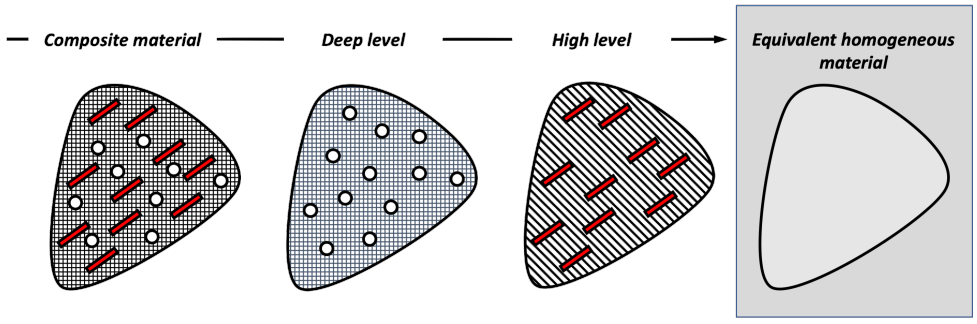

Figure 3.1: Two-level method. A first composite is considered as a matrix with cavities (deep level). The latter homogenized material is used as a matrix where short fibers are embedded (high level). The homogenization of this material gives the final equivalent homogeneous material.

When using Abaqus (2019) to homogenize the composite at the high level, we need to introduce the

mechanical properties of the homogenized matrix from the deep level. The problem is that Abaqus (2019) ask for all 3D engineering constants as input for the matrix phase material. In order to compute those missing properties (only 2D simulations are considered for the deep level as well as for the high level), we need to compute them with 3D full-field. This is done using Digimat-FE. The latter input composite will be only composed by a matrix phase containing random cylindrical cavities, i.e. the homogenized material will be transversely isotropic. We have to be careful when using engineering constants from Digimat-FE to Abaqus since the global axes are not defined the same way in both software's. Note that we also have to model this random geometry three times to get averaged results. The latter averaged properties are given in table 3.1.

v_p [%]	$\overline{E}_3$ [MPa]	$\overline{\nu}_{31}$ [-]	$\overline{\nu}_{32}$ [-]	$\overline{G}_{23}$ [MPa]	$\overline{G}_{13}$ [MPa]
1	3072.8	0.35	0.35	1131.8	1131.5
4	2991.3	0.35	0.35	1083.1	1082.9
7	2909.5	0.35	0.35	1035.4	1034.9
10	2827.8	0.35	0.35	989.7	987.6

Table 3.1: Out-of-plane mechanical properties of the transversely isotropic two-phase material composed by a matrix and cavities, computed with Digimat-FE

We can compare the results with the law of mixture. It is based on the assumption that both materials contribute to the stiffness of the composite in proportion to their respective moduli and fractional volumes. By the classical rule of mixture for a matrix with some porosity :

$$\overline{E}_{3,mix} = E_m(1 - v_p) \tag{3.1}$$

Several authors developed rules based on different assumptions. Choren et al. (2013) gives a complete review of the existing models. We took and put some of them in table 3.2 to compare them with the 3D results from table 3.1, using rounded final values. Fryxell and Hasselman models are based on linear equation, McAdam on power equations, and Hashin on other equations (see above mentioned review for more details).

v_p [%]	$\overline{E}_{3,3D}$ [MPa]	$\overline{E}_{3,mix}$ [MPa]	$\overline{E}_{3,Hashin}$ [MPa]	$\overline{E}_{3,Hasselman}$ [MPa]	$\overline{E}_{3,Fryxell}$ [MPa]	$\overline{E}_{3,McAdam}$ [MPa]	$\overline{E}_{3,Ramakrishnan}$ [MPa]
1	3073	3069	3097	3097	3041	2996	3068
4	2991	2976	3052	3053	2864	2698	2961
7	2909	2883	2964	2968	2688	2422	2838
10	2828	2790	2844	2849	2511	2167	2700

Table 3.2: Out-of-plane mechanical properties of the transversely isotropic two-phase material composed by a matrix and cavities, computed with Digimat-FE

2 Parametric study

Here we present results from different homogenization techniques we introduced before.

2.1 Direct Finite Element Analysis (FEA) without cavities

In what follows we will use Naili et al. (2019) results on a 2D RVE as reference point to compare and evaluate the models. The RVE microstructures depicted on Figures 3.2a to 3.2c are generated using

Digimat-FE software. The randomly positioned fibers are ellipsoidal shaped and orientated along the x-axis with an aspect ratio $A_R = 24$. They are embedded in the matrix phase depicted with a clear background on the aforementioned figures. The RVEs are 200x200 sized compared to the fiber length fixed at 24 and are available for $v_f = 10\%$, 16% and 30%.

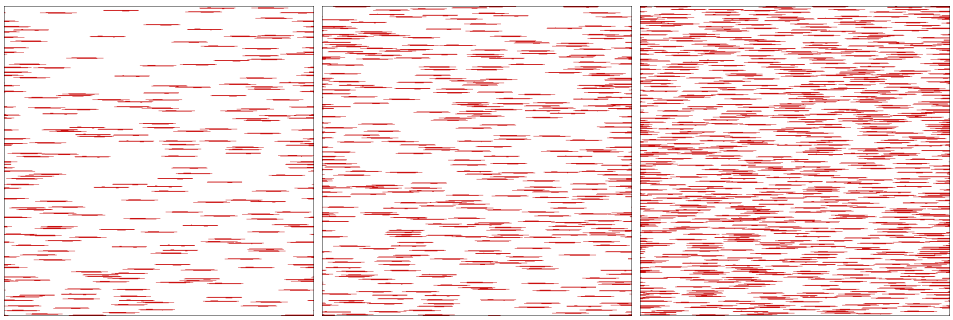

(a) $v_f = 10\%$ (b) $v_f = 16\%$ (c) $v_f = 30\%$

Figure 3.2: Several microstructures of the RVE with random placement aligned fibers fraction of $v_f = 10\%$, $v_f = 16\%$ and $v_f = 30\%$.

The microstructures depicted here above are meshed using free meshing techniques to respect closely the shape of the fibers and are composed of C2D4R[1] and C2D3[2] elements. The latter are mainly distributed around sharp edges like the fiber tips. After a convergence study the authors came up with meshes using around 71000 elements.

Now we recall some important details about the boundary conditions the authors imposed on the boundary. They used kinematic uniform boundary conditions (KUBC), a Dirichlet type of uniform boundary condition, applied through the strain tensor. This type of boundary condition is more convenient since the mesh is generated using free meshing technique. It means that the uneven distribution of the nodes along the boundaries make difficult to impose periodic boundary condition since it would require the pairing of homologous nodes as it was explained on section 3.1 in chapter 1. Finally the authors assumed plane stress over all the studied cases.

In what follows note that simulation results are rounded to the closest decimal while the error is computed using non rounded values. Each effective engineering constant is normalized by the related matrix elastic constant, this gives the following notation : $\overline{E}_1^*$, $\overline{E}_2^*$, $\overline{\nu}_{12}^*$ and $\overline{G}_{12}^*$. Results from tables 3.3 to 3.5 globally present an error[3] less than 5%, expect for $\overline{\nu}_{12}$ coefficient in the case of $v_f = 30\%$ which is higher than the accepted 5%. We can conclude that the unit cell we use give sufficiently good results.

[1] 4 nodes quadrilateral elements with reduced integration

[2] 3 nodes triangular elements with complete integration

[3] The error is defined the following :

$$error = \frac{\text{RVE} - \text{Cell}}{\text{RVE}}$$

	RVE [−]	Unit Cell [−]	Error [%]
$\overline{E}_1^*$	2.12	2.12	0.16
$\overline{E}_2^*$	1.19	1.18	0.88
$\overline{\nu}_{12}^*$	0.99	1.00	1.2
$\overline{G}_{12}^*$	1.12	1.11	0.91

Table 3.3: Plane stress results for a volume fraction of $v_f = 10\%$ of fibers.

	RVE [−]	Unit Cell [−]	Error [%]
$\overline{E}_1^*$	2.96	3.02	2.19
$\overline{E}_2^*$	1.29	1.29	0.5
$\overline{\nu}_{12}^*$	0.99	0.98	1.13
$\overline{G}_{12}^*$	1.20	1.19	0.77

Table 3.4: Plane stress results for a volume fraction of $v_f = 16\%$ of fibers.

	RVE [−]	Unit Cell [−]	Error [%]
$\overline{E}_1^*$	5.36	5.42	1.1
$\overline{E}_2^*$	1.57	1.57	0.02
$\overline{\nu}_{12}^*$	0.98	0.92	6.68
$\overline{G}_{12}^*$	1.46	1.43	2.26

Table 3.5: Plane stress results for a volume fraction of $v_f = 30\%$ of fibers.

Before going any further we compared the latter results with a 3D unit cell (figure 3.3). The tests are carried in Digimat-FE. Material properties and geometries are taken exactly the same as the previous computations. The fibers are modeled by simple cylinders to stay as close as possible as the shape of those fibers chosen for the 2D models. Using default parameters in Digimat-FE, we get 46 245, 49 251 and 51 063 elements for $v_f = 10\%$, 16% and 30% respectively. Due to the simple shape of the fibers we do not need any refinement of the mesh.

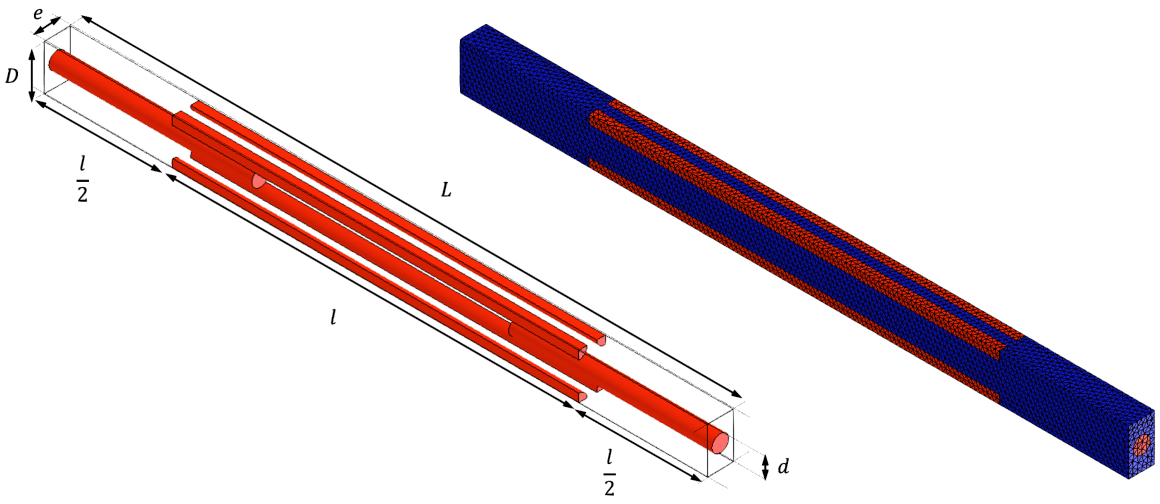

Figure 3.3: 3D Unit Cell model using Digimat-FE and its associated mesh. Case $v_f = 23\%$, mesh with 51063 elements (C3D10).

From tables 3.6 to 3.8, where results are presented the same way we did just here above, we can see that 3D do not specially lie between 2D plane stress and strain. Still, globally 3D results are closer to 2D plane strain than 2D plane stress consideration.

	2D RVE [−]	2D Unit Cell (Plane Stress) [−]	2D Unit Cell (Plane Strain) [−]	3D Unit Cell [−]
$\overline{E}_1^*$	2.12	2.12	2.31	2.78
$\overline{E}_2^*$	1.19	1.18	1.46	1.26
$\overline{G}_{12}^*$	1.12	1.11	1.11	1.19

Table 3.6: Results for a volume fraction of $v_f = 10\%$ of fibers. (3D : 46 245 elements)

	2D RVE [−]	2D Unit Cell (Plane Stress) [−]	2D Unit Cell (Plane Strain) [−]	3D Unit Cell [−]
$\overline{E}_1^*$	2.96	3.02	3.28	4.14
$\overline{E}_2^*$	1.29	1.29	1.65	1.42
$\overline{G}_{12}^*$	1.20	1.19	1.19	1.32

Table 3.7: Results for a volume fraction of $v_f = 16\%$ of fibers. (3D : 49 251 elements)

	2D RVE [−]	2D Unit Cell (Plane Stress) [−]	2D Unit Cell (Plane Strain) [−]	3D Unit Cell [−]
$\overline{E}_1^*$	5.36	5.42	5.85	6.87
$\overline{E}_2^*$	1.58	1.57	2.09	1.91
$\overline{G}_{12}^*$	1.46	1.43	1.43	1.69

Table 3.8: Results for a volume fraction of $v_f = 30\%$ of fibers. (3D : 51 063 elements)

2.2 Direct Finite Element Analysis (FEA) with cavities

From Figures 3.4 to 3.7 we study the influence of the porosity on the mechanical properties of the material and compare it with the previous case without cavity. We can see that the porosity has a strong impact on the mechanical properties of the material. Engineering constants $\overline{E}_2$ and $\overline{G}_{12}$ are more impacted by the effect of the porosity than the other ones. This is simply due to the orientation of the fibers aligned with respect to direction 1. Note that some point at $c_f = 16\%$ seems to present some inconsistency at $c_p = 4\%$ when we compare it with the other curves. Poisson coefficient does not present any stiff evolution. Still, when we increase the fibers volume fraction, the material seems to become more sensible to the effect of the porosity.

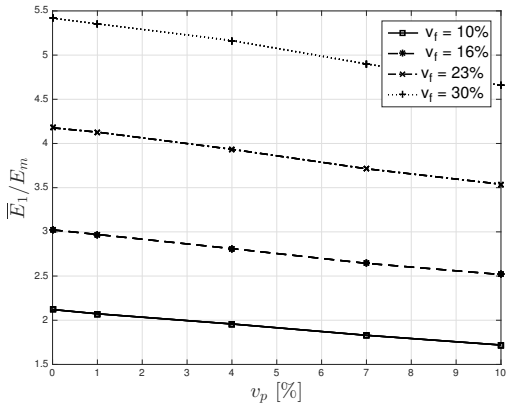

Figure 3.4: Plane stress results for $\overline{E}_1^*$ with porosity v_p ranging 1% to 10% and fibers volume fraction 10% to 30%, compared to the homogeneous reinforced matrix.

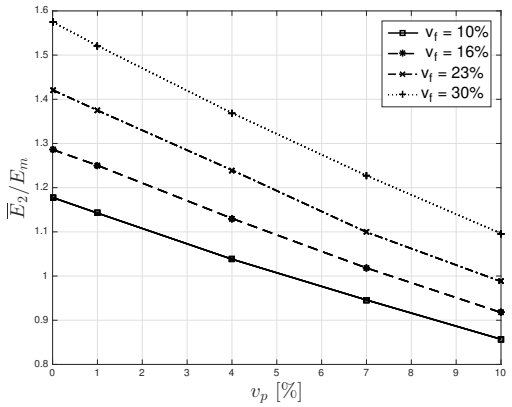

Figure 3.5: Plane stress results for $\overline{E}_2^*$ with porosity v_p ranging 1% to 10% and fibers volume fraction 10% to 30%, compared to the homogeneous reinforced matrix.

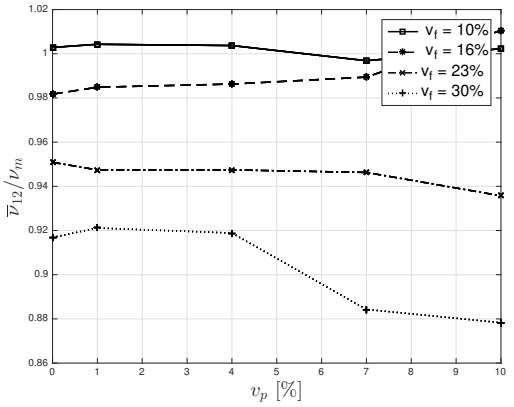

Figure 3.6: Plane stress results for $\overline{\nu}_{12}^*$ with porosity v_p ranging 1% to 10% and fibers volume fraction 10% to 30%, compared to the homogeneous reinforced matrix.

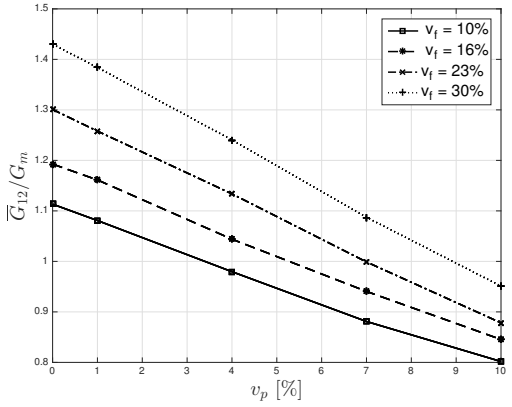

Figure 3.7: Plane stress results for $\overline{G}_{12}^*$ with porosity v_p ranging 1% to 10% and fibers volume fraction 10% to 30%, compared to the homogeneous reinforced matrix.

2.3 Direct Finite Element Analysis (FEA) vs. 2-level homogenization

Here we compare results from direct FEA with the 2-level homogenization under plane stress consideration, methods that we introduced before. Following the different results showed on tables 3.9 to 3.12, we can conclude by looking at the relative differences[4] an excellent agreement between the two methods with errors below 2%. Note that this relative difference is ever smaller for the Poisson coefficient that gives relative difference around 10^{-5}.

[4] Relative difference is defined the same way we previously defined the error.

v_f [%]	v_p [%]	Direct FEA [−]	2-level [−]	Rel. Diff. [%]
10	1	2.07	2.08	0.19
10	4	1.96	1.95	0.57
10	7	1.83	1.82	0.31
10	10	1.72	1.7	0.89
16	1	2.97	2.97	0
16	4	2.81	2.81	0.14
16	7	2.64	2.66	0.78
16	10	2.52	2.52	0.05
23	1	4.13	4.12	0.27
23	4	3.93	3.94	0.07
23	7	3.71	3.76	1.26
23	10	3.54	3.58	1.25
30	1	5.35	5.35	0.03
30	4	5.16	5.15	0.2
30	7	4.9	4.96	1.16
30	10	4.66	4.76	2.08

Table 3.9: $\overline{E}_1^*$ results comparison between direct FEA method and 2-level procedure homogenization under plane stress consideration.

v_f [%]	v_p [%]	Direct FEA [−]	2-level [−]	Rel. Diff. [%]
10	1	1.14	1.14	0.1
10	4	1.04	1.05	0.6
10	7	0.95	0.96	0.77
10	10	0.86	0.88	1.45
16	1	1.25	1.25	0.02
16	4	1.13	1.15	0.59
16	7	1.02	1.05	1.15
16	10	0.92	0.96	1.85
23	1	1.37	1.38	0.16
23	4	1.24	1.27	0.72
23	7	1.1	1.16	1.61
23	10	0.99	1.07	2.2
30	1	1.52	1.53	0.19
30	4	1.37	1.41	0.72
30	7	1.23	1.29	1.2
30	10	1.1	1.18	1.83

Table 3.10: $\overline{E}_2^*$ results comparison between direct FEA method and 2-level procedure homogenization under plane stress consideration.

v_f [%]	v_p [%]	Direct FEA [−]	2-level [−]	Rel. Diff. [%]
10	1	1	1	$< 10^{-5}$
10	4	1	1	$< 10^{-5}$
10	7	1	1	$< 10^{-5}$
10	10	1	1.01	$< 10^{-5}$
16	1	0.98	0.98	$< 10^{-5}$
16	4	0.99	0.98	$< 10^{-5}$
16	7	0.99	0.98	$< 10^{-5}$
16	10	1.01	0.99	$< 10^{-5}$
23	1	0.95	0.95	$< 10^{-5}$
23	4	0.95	0.95	$< 10^{-5}$
23	7	0.95	0.95	$< 10^{-5}$
23	10	0.94	0.95	$< 10^{-5}$
30	1	0.92	0.92	$< 10^{-5}$
30	4	0.92	0.92	$< 10^{-5}$
30	7	0.88	0.92	$< 10^{-5}$
30	10	0.88	0.92	$< 10^{-5}$

Table 3.11: $\overline{\nu}_{12}^*$ results comparison between direct FEA method and 2-level procedure homogenization under plane stress consideration.

v_f [%]	v_p [%]	Direct FEA [−]	2-level [−]	Rel. Diff. [%]
10	1	1.08	1.08	0.02
10	4	0.98	0.99	0.21
10	7	0.88	0.91	0.49
10	10	0.8	0.83	0.51
16	1	1.16	1.16	0.03
16	4	1.04	1.06	0.23
16	7	0.94	0.97	0.41
16	10	0.85	0.88	0.58
23	1	1.26	1.26	0.06
23	4	1.13	1.16	0.23
23	7	1	1.06	0.59
23	10	0.88	0.97	0.91
30	1	1.38	1.39	0.04
30	4	1.24	1.27	0.25
30	7	1.09	1.17	0.59
30	10	0.95	1.06	0.88

Table 3.12: $\overline{G}_{12}^*$ results comparison between direct FEA method and 2-level procedure homogenization under plane stress consideration.

Chapter 4

Porous composites with misaligned short fibers reinforcement

1 Modeling of misaligned fibers

We consider now a multi-phase material RVE containing a matrix (which may contain some porosity) and short fibers of same shape but different orientations this time. We will use in this chapter the so-called 2-step homogenization procedure (see sections 2.2 and 3.2 of the present chapter). We'll see that it requires to decompose the multi-phase material RVE into several so-called UD pseudo-grains (PG), made of a matrix material and aligned inclusions (more details in what follows).

1.1 Orientation Distribution Function (ODF)

Before proceeding to the homogenization of the pseudo-grains, it is necessary to introduce some tools that will make it possible to describe the orientation of the fibers within each volume element. In 3D a unit vector $\mathbf{p}$ along the axis of revolution of a fiber can be described by two spherical angle θ and ϕ (see figure 4.1). In 2D, within the global Cartesian system (O,X,Y), i.e. (O,1,2) on the figure, the orientation of each fiber is described by its angle ϕ angle with respect to the X-axis.

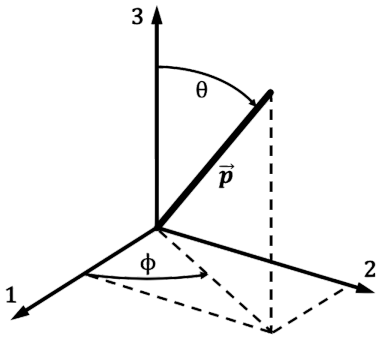

Figure 4.1: Fiber orientation (3D)

Since $\mathbf{p}$ varies from fiber to fiber within the same RVE, we introduce the notion of orientation distribution function (ODF), $\psi(\mathbf{p})$.
By definition $\psi(\mathbf{p})d\mathbf{p}$ is the probability of finding fibers within the solid angles $[\mathbf{p}, \mathbf{p} + d\mathbf{p}]$.

Each ODF obeys the following conditions :

- $\psi(\mathbf{p}) = \psi(-\mathbf{p})$: i.e. two opposed vectors define unique indistinguishable inclusions

- $\oint \psi(\mathbf{p})d\mathbf{p} = 1$: i.e. a normalization condition that imposes the sum of probabilities equal 1

Now we can homogenize the RVE of the composite if the ODF is known. A description of the average orientation distribution is expressed by orientation tensors (Advani and Tucker (1987)) . The so-called second-rank orientation tensor, $\mathbf{a}$ is the statistical second-order moment of the orientation field $\mathbf{p}$. In 2D, its components are :

$$a_{ij} = \int_0^{2\pi} p_i p_j \psi(\phi) d\phi \equiv \langle p_i p_j \rangle_\phi \tag{4.1}$$

This tensor gives information about the average orientation of the inclusions inside the RVE and verifies the following condition :

$$a_{ij} = a_{ji} \tag{4.2}$$

with a_{11}, $a_{22} \geq 0$ and $a_{11} + a_{22} = 1$.

The study case of this work is in 2D, and supposes :

$$\mathbf{a} = \begin{pmatrix} a & 0 \\ 0 & 1-a \end{pmatrix}_{(\mathbf{e}_x, \mathbf{e}_y)}$$

Some special cases may be mentioned (see figure 4.2) :

- case $a = 1$ ($a_{11} = 1$; $a_{22} = 0$) : aligned orientation in direction 1,
- case $a = 1$ ($a_{11} = 0$; $a_{22} = 1$) : aligned orientation in direction 2,
- case $a = 0.5$ ($a_{11} = a_{22} = 0$) : perfectly random orientation in 2D.

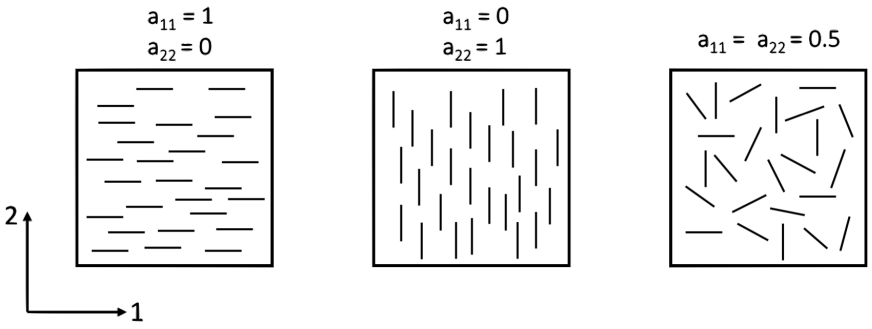

Figure 4.2: Particular orientations of the fibers in function of the orientation tensor $\mathbf{a}$.

For $a \in]0;1[$ we will construct the ODF according to the "Natural Closure Approximation" from Verleye and Dupret (1993,1995) :

$$\psi(\phi) = \frac{\frac{1}{2\pi}}{\frac{1-a}{a}\cos^2(\phi) + \frac{a}{1-a}\sin^2(\phi)} \tag{4.3}$$

We consider the parameter a ranging from 0.2 to 0.8 (see figure 4.3).

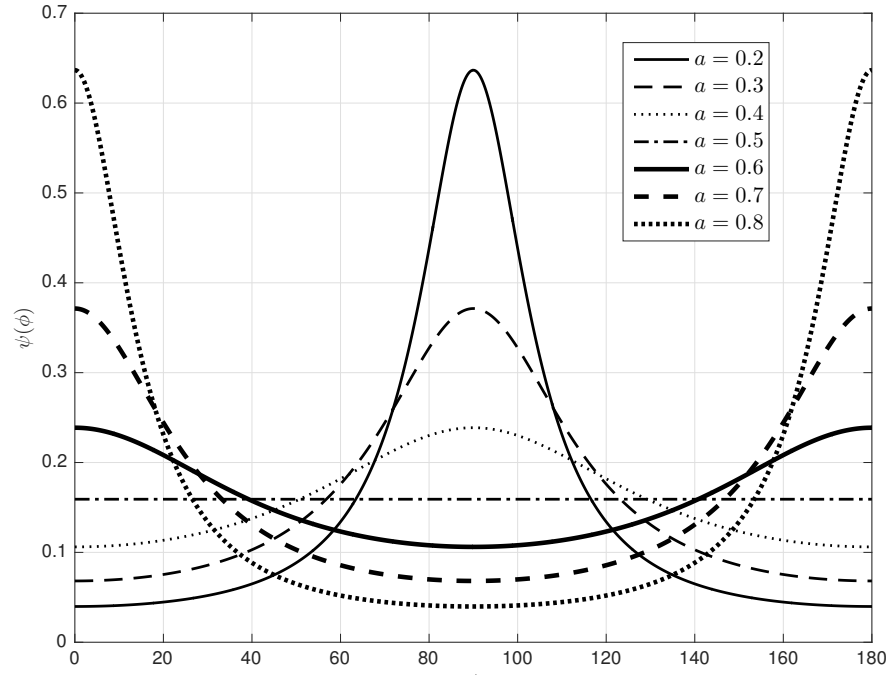

Figure 4.3: Evolution of the orientation distribution function with ϕ

From now on, we are in plane stress consideration.

1.2 ODF discretization

For a fixed value of a, we still need to discretize interval $[0; 180]$[1] into $N > 2$ sub-intervals of length $\Delta\phi$ in order to discretize $\psi(\phi)$.
For each discrete orientation ϕ_i inside the composite, we link a weight w_i defined as :

$$w_i = 2\psi(\phi_i)\Delta\phi \tag{4.4}$$

with $\phi_i = i\Delta\phi$, $i = 1...N$.

One last step consists of computing the number of sub-intervals in order to guarantee a sufficiently fine discretization of the interval. To do so we define a threshold ϵ such that :

- If $|\Sigma_i w_i - 1| < \epsilon$: the number of sub-intervals is large enough. Then we proceed to normalisation of the weight like this :

$$w_i = \frac{w_i}{\Sigma_i w_i} \tag{4.5}$$

- If $|\Sigma_i w_i - 1| > \epsilon$: the number of sub-intervals is not large enough and we need to refine it.

The ideal case is obviously the one for which $\Sigma_i w_i = 1$, requiring an infinite number of sub-intervals, hence the notion of treshold previously introduced here above.

[1] We consider only this half interval due to condition $\psi(\boldsymbol{p}) = \psi(-\boldsymbol{p})$.

Figure 4.4 gives the evolution of the sum of those weights as function of the number of sub-intervals for the 30 first sub-intervals. If we fix a threshold for the precision of the discretization $\epsilon = 10^{-5}$, we find for each orientation tensor the following results :

a	0.2	0.3	0.4	0.5	0.6	0.7	0.8
N	2501	4287	6668	10001	15002	23335	40001

Table 4.1: Number of sub-intervals required for each orientation tensors to reach a precision of $\epsilon = 10^{-5}$ for the ODF discretization.

Very large values are obtained to reach this fixed threshold as we are interested in accurate but not especially optimized results.

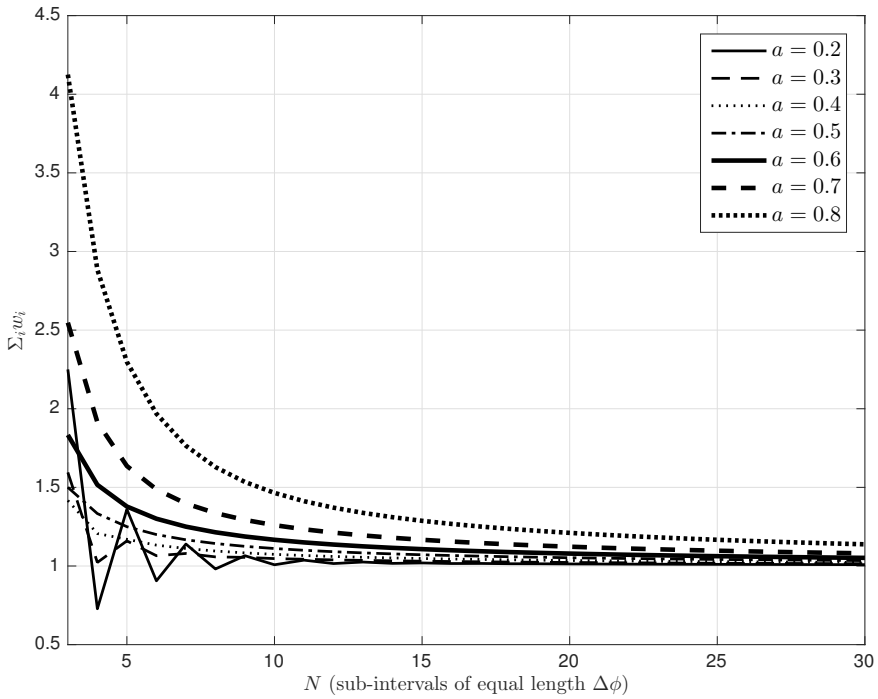

Figure 4.4: Evolution of the sum of the weights w_i as function of the discretization of the interval $[0; 180]$

Ogierman and Kokot (2017) proposed an approach that leads to reduction of the number of discrete orientations based on optimal selection of discrete orientations and corresponding weights. They concluded with more computationally efficient homogenization results, especially in the case of inelastic materials. For instance they showed that with an amount of nine pseudo-grains is sufficient for an appropriate representation of orientation distribution. Still due to the optimization computations they underlined that, in general, it requires more computational effort than the method of orientation distribution reconstruction we apply here.

2 Matrix with misaligned short fibers, no cavities

2.1 Direct FE analysis on RVE

When considering misaligned short-fibers reinforcement matrix with no cavities, we need to compare the models (see parametric study results on section 4.1) with reference results. Naili et al. (2019). did RVE computations considering fiber volume fraction of $v_f = 10\%$, 16% and 30% and will be used as reference points. The modeling of their RVE and the mesh they used are described in what follows.

RVE Generation

The microstructure of the 2D RVE's from Naili et al. (2019) depicted on Figures 4.5a to 4.5d have been generated using Digimat-FE software. The microstructures are 200x200 sized RVEs. Fibers are oriented by means of a built-in ODF function according to the orientation tensor where a_{11} varies from 0.5 (2D random orientation) to 0.8 with fiber's volume fraction $v_f = 10\%$, 16% and 30%. The generated RVE models are given in Figure 4.5 for $v_f = 10\%$. The authors mention they could not generate enough models in the considered interval (only the case of $a_{11} = 0.8$ was achievable) when $v_f = 30\%$ due to the percolation threshold. It means that at some point it was impossible for them to generate the microstructure without fibers overlapping. For this reason we will only use the studied microstructures with 10% and 16% fiber's volume fraction as reference point in what follows. The microstructures presented here below are mentioned as using the same mesh and boundary conditions than in the aligned SFRC studied case in section 2.1 of chapter 3, also under plane stress consideration.

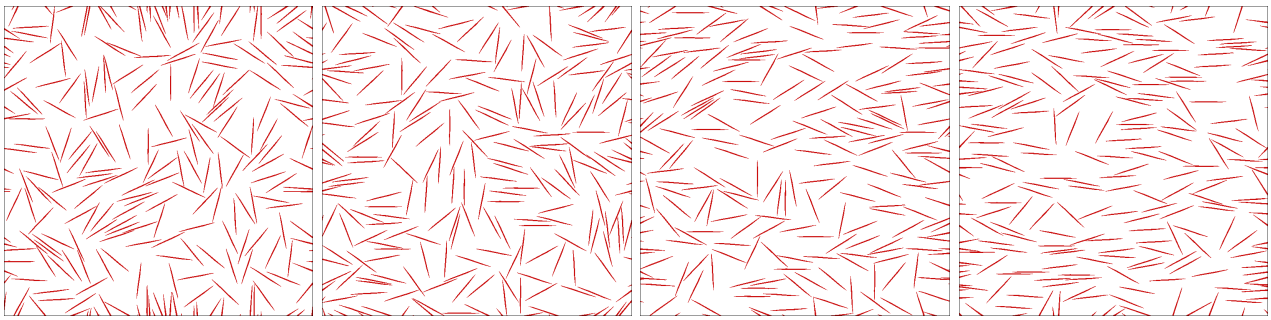

(a) $a_{11} = 0.5$ (b) $a_{11} = 0.6$ (c) $a_{11} = 0.7$ (d) $a_{11} = 0.8$

Figure 4.5: Several microstructures of the RVE with a misaligned fibers fraction of $v_f = 10\%$, as function of the orientation tensor component a_{11}.

2.2 Two-step FE homogenization with two-phase PGs

The 2-step method consists in decomposing the RVE into infinitesimal grains. Each pseudo-grain (PG) is unidirectional (UD) and characterized by a different orientation tensor $\boldsymbol{p}$, i.e. the fibers are oriented in the same direction. In what follows we will consider two different cases : short fiber reinforced matrix with and without porosity.
The method consists in two steps (see figure 4.6 :

- Step 1 : homogenization of each PG individually,
- Step 2 : homogenization of the aggregate composed by all the PGs.

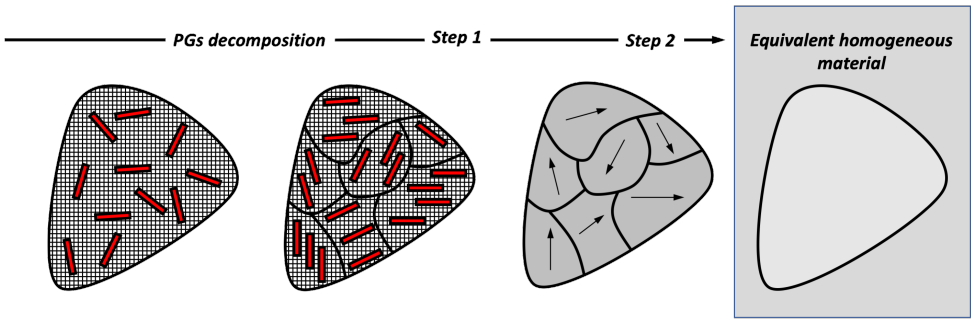

Figure 4.6: Two-step method. First step : UD two-phase PGs decomposition. Step 2 : homogenization of the aggregate composed of the homogenized UD two-phase PGs. The homogenization of this material gives the final equivalent homogeneous material.

2.2.1 First step : homogenization of each two-phase UD pseudo-grain

In the case of a matrix with misaligned short fibers without cavities, each PG is made of a matrix material reinforced with fibers oriented in the same direction. The fibers have the same shape and aspect ratio.

In this first step, each PG is a two-phase composite which contains the same volume fraction of matrix as in RVE, v_0, and those inclusions of volume fraction $1 - v_0$. The effective engineering properties of the PG are obtained by FEA on the UD unit cell of section 2.1 in chapter 2.

2.2.2 Second step : homogenization of the aggregate

In this second step the RVE is considered as an aggregate of homogenized PG (i). Each grain (i) is characterized by a stiffness $\overline{\boldsymbol{C}}_{i,\boldsymbol{p}}$ computed by FEA during the first step and an orientation tensor $\boldsymbol{p}$. The PG effective properties are weighted by an orientation distribution function $\psi(\boldsymbol{p})$. In this work we will use three homogenization methods introduced in section 6.2 in chapter 3 during step two.

First method : FE-Voigt

The model assumes that the strain field is uniform inside the aggregate. The macro stiffness is given by :

$$\overline{\boldsymbol{C}} = \langle \overline{\boldsymbol{C}}_{i,\boldsymbol{p}} \rangle_{i,\phi_i} \tag{4.6}$$

Numerically it means that the approximate macro stiffness matrix is computed using :

$$[\overline{\boldsymbol{C}}] = \sum_i w_i [\overline{\boldsymbol{C}}^{(i)}] \tag{4.7}$$

with w_i the weight of the orientation angle ϕ_i of the PG (i). The stiffness matrix $[\overline{\boldsymbol{C}}^{(i)}]$ of the PG (i) is the UD two-phase unit cell's stiffness matrix obtained by FEA but rotated (see section 2.3) by an angle ϕ_i to express all the local stiffness matrices in the same global frame and to sum them up correctly.

Second method : FE-Reuss

The model assumes that the stress field is uniform inside the aggregate. The macro stiffness is given by :

$$\overline{\boldsymbol{C}} = (\langle (\overline{\boldsymbol{C}}_{i,\boldsymbol{p}})^{-1} \rangle_{i,\phi_i})^{-1} \tag{4.8}$$

Numerically it means that the approximate macro stiffness matrix is computed using the compliance matrix whose expression is :

$$[\overline{\boldsymbol{S}}] = \sum_i w_i [\overline{\boldsymbol{S}}^{(i)}] \tag{4.9}$$

with w_i the weight of the orientation angle ϕ_i of the PG (i). The compliance matrix $[\overline{\boldsymbol{S}}^{(i)}]$ of the PG (i) is the UD two-phase unit cell's compliance matrix obtained by FEA but rotated (see section 2.3) by an angle ϕ_i to express all the local stiffness matrices in the same global frame and to sum them up correctly.

Third method : FE-MT

This third method is an FE homogenization model inspired by Mori-Tanaka. Following Benveniste's interpretation of the latter model each inclusion can be seen as if it were isolated in an infinite matrix that undergoes a far-field strain field equal to the average matrix strain in the real RVE.
A particularly interesting result from Pierard et al. (2004) is that for misaligned inclusions the direct M-T homogenization is a special case of the pseudo-grain decomposition method, i.e. 2-step method, which corresponds to :

$$\langle \boldsymbol{\varepsilon} \rangle_{\omega_i^0, \boldsymbol{p}} = \langle \boldsymbol{\varepsilon} \rangle_{\omega^0} \tag{4.10}$$

where ω^0 and ω_i^0 stand for the matrix domains respectively in the RVE and within a pseudo-grain (i). Therefore direct Mori-Tanaka is a particular case of the pseudo-grain decomposition method, which corresponds to :

$$\langle \boldsymbol{\varepsilon} \rangle_{\omega_{i,\boldsymbol{p}}^0} = \langle \boldsymbol{\varepsilon} \rangle_{\omega_0}, \forall \text{ pseudo-grain } (i, \boldsymbol{p}) \tag{4.11}$$

Using relation 4.11, we can express the average strain inside the RVE as :

$$\begin{aligned}
\langle \boldsymbol{\varepsilon} \rangle_{\omega} &= \langle v_0 \langle \boldsymbol{\varepsilon} \rangle_{\omega_i^0} + (1 - v_0) \langle \boldsymbol{\varepsilon} \rangle_{\omega_i^1} \rangle_i \\
&= \langle (v_0 \boldsymbol{I} + (1 - v_0) \boldsymbol{B}_i^{\boldsymbol{\varepsilon}}) : \langle \boldsymbol{\varepsilon} \rangle_{\omega_i^0} \rangle_i \\
&= \langle (v_0 \boldsymbol{I} + (1 - v_0) \boldsymbol{B}_i^{\boldsymbol{\varepsilon}}) \rangle_i : \langle \boldsymbol{\varepsilon} \rangle_{\omega^0} \\
&= (v_0 \boldsymbol{I} + (1 - v_0) \langle \boldsymbol{B}_i^{\boldsymbol{\varepsilon}} \rangle_i) : \langle \boldsymbol{\varepsilon} \rangle_{\omega^0}
\end{aligned} \tag{4.12}$$

If we do the same for the average stress field :

$$\begin{aligned}
\langle \boldsymbol{\sigma} \rangle_{\omega} &= \langle v_0 \langle \boldsymbol{\sigma} \rangle_{\omega_i^0} + (1 - v_0) \langle \boldsymbol{\sigma} \rangle_{\omega_i^1} \rangle_i \\
&= \langle (v_0 \boldsymbol{C}_0 + (1 - v_0) \boldsymbol{C}_i : \boldsymbol{B}_i^{\boldsymbol{\varepsilon}}) : \langle \boldsymbol{\varepsilon} \rangle_{\omega_i^0} \rangle_i \\
&= \langle (v_0 \boldsymbol{C}_0 + (1 - v_0) \boldsymbol{C}_i : \boldsymbol{B}_i^{\boldsymbol{\varepsilon}}) \rangle_i : \langle \boldsymbol{\varepsilon} \rangle_{\omega^0} \\
&= (v_0 \boldsymbol{C}_0 + (1 - v_0) \langle \boldsymbol{C}_i : \boldsymbol{B}_i^{\boldsymbol{\varepsilon}} \rangle_i) : \langle \boldsymbol{\varepsilon} \rangle_{\omega^0}
\end{aligned} \tag{4.13}$$

By putting equations 4.12 and 4.13 in the constitutive Hooke's law, we easily get the following expression for the macro stiffness of the whole aggregate :

$$\overline{\boldsymbol{C}} = (v_0 \boldsymbol{C}_0 + (1 - v_0) \langle \boldsymbol{C}_i : \boldsymbol{B}^{\boldsymbol{\varepsilon}} \rangle_i) : (v_0 \boldsymbol{I} + (1 - v_0) \langle \boldsymbol{B}_i^{\boldsymbol{\varepsilon}} \rangle_i)^{-1} \tag{4.14}$$

If we homogenize a UD pseudo-grain with full-field using FE homogenization, we don't have to use analytical formula for Mori-Tanaka.

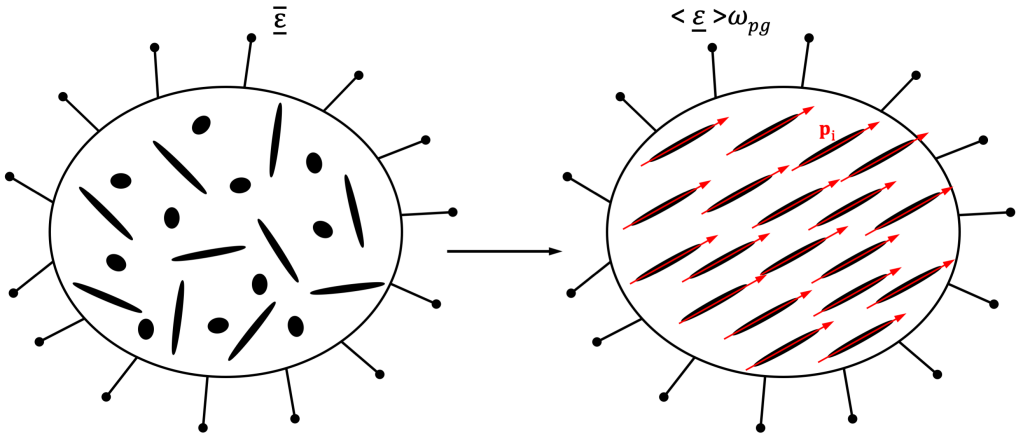

Figure 4.7: Homogenization of a UD pseudo-grain with full-field method (FEA) does not require to use analytical formula for Mori-Tanaka.

Using a simple notation :

$$\langle \boldsymbol{\varepsilon} \rangle_{\omega^1_{p.g.}} = \boldsymbol{A}^{\boldsymbol{\varepsilon}}_{p.g.} : \langle \boldsymbol{\varepsilon} \rangle_{\omega_{p.g.}} \tag{4.15}$$

with $\boldsymbol{A}^{\boldsymbol{\varepsilon}}_{p.g.}$, the strain concentration tensor of the pseudo-grain.

We use the relation between average stress and strain :

$$\langle \boldsymbol{\sigma} \rangle_{\omega_{p.g.}} = \overline{\boldsymbol{C}}_{p.g.} : \langle \boldsymbol{\varepsilon} \rangle_{\epsilon_{p.g.}} \tag{4.16}$$

where $\overline{\boldsymbol{C}}_{p.g.}$, the macro stiffness of the UD pseudo-grain, is computed using FE analysis.

Therefore, we can express $\boldsymbol{A}^{\boldsymbol{\varepsilon}}_{p.g.}$ as function of the stiffness matrices as follow.

Recalling $\langle \boldsymbol{\varepsilon} \rangle_{\omega_{p.g.}} = v_0 \langle \boldsymbol{\varepsilon} \rangle_{\omega_0} + (1 - v_0) \langle \boldsymbol{\varepsilon} \rangle_{\omega_1}$ and using eq. 4.15 :

$$\langle \boldsymbol{\varepsilon} \rangle_{\omega_0} = \frac{1}{v_0} (\boldsymbol{I} - (1 - v_0) \boldsymbol{A}^{\boldsymbol{\varepsilon}}_{p.g.}) : \langle \boldsymbol{\varepsilon} \rangle_{\omega} \tag{4.17}$$

By definition,

$$\langle \boldsymbol{\sigma} \rangle_{\omega_{p.g.}} = v_0 \langle \boldsymbol{\sigma} \rangle_{\omega_0} + (1 - v_0) \langle \boldsymbol{\sigma} \rangle_{\omega_1} \tag{4.18}$$

where average stress field in each phase is defined by $\langle \boldsymbol{\sigma} \rangle = \overline{\boldsymbol{C}} : \langle \boldsymbol{\varepsilon} \rangle$.

Using equation 4.18 and the expression of the macro stiffness and equation 4.17, we have :

$$\boldsymbol{C}_{p.g.} : \langle \boldsymbol{\varepsilon} \rangle_{\omega} = v_0 \boldsymbol{C}_0 : \langle \boldsymbol{\varepsilon} \rangle_{\omega_0} + v_1 \boldsymbol{C}_1 : \langle \boldsymbol{\varepsilon} \rangle_{\omega_1} \tag{4.19}$$

Finally, the stiffness of the pseudo-grain is given by :

$$\boldsymbol{C}_{p.g.} = \boldsymbol{C}_0 + (1 - v_0)(\boldsymbol{C}_1 - \boldsymbol{C}_0) : \boldsymbol{A}^{\boldsymbol{\varepsilon}}_{p.g.} \tag{4.20}$$

Reorganising the terms leads to :

$$\boldsymbol{A}^{\boldsymbol{\varepsilon}}_{p.g.} = \frac{1}{1 - v_0} (\boldsymbol{C}_1 - \boldsymbol{C}_0)^{-1} : (\overline{\boldsymbol{C}}_{p.g.} - \boldsymbol{C}_0) \tag{4.21}$$

On the other hand and again using a simple notation :

$$\langle \boldsymbol{\varepsilon} \rangle_{\omega^1_{p.g.}} = \boldsymbol{B}^{\boldsymbol{\varepsilon}}_{p.g.} : \langle \boldsymbol{\varepsilon} \rangle_{\omega^0_{p.g.}} \tag{4.22}$$

with $\boldsymbol{B}^{\boldsymbol{\varepsilon}}_{p.g.}$, the strain concentration tensor.

So :

$$\boldsymbol{A}^{\boldsymbol{\varepsilon}}_{p.g.} : \langle \boldsymbol{\varepsilon} \rangle_{\omega_{p.g.}} = \boldsymbol{B}^{\boldsymbol{\varepsilon}}_{p.g.} : \frac{1}{v_0}(\boldsymbol{I} - (1 - v_0)\boldsymbol{A}^{\boldsymbol{\varepsilon}}_{p.g.}) : \langle \boldsymbol{\varepsilon} \rangle_{\omega_{p.g.}} \tag{4.23}$$

Leading to :

$$\boldsymbol{B}^{\boldsymbol{\varepsilon}}_{p.g.} = v_0 \boldsymbol{A}^{\boldsymbol{\varepsilon}} : (\boldsymbol{I} - (1 - v_0)\boldsymbol{A}^{\boldsymbol{\varepsilon}}_{p.g.})^{-1} \tag{4.24}$$

We can finally express $\boldsymbol{B}^{\boldsymbol{\varepsilon}}_{p.g.}$ using eqs. 4.24 and 4.21 :

$$\boldsymbol{B}^{\epsilon}_{p.g.} = \frac{v_0}{1 - v_0}(\boldsymbol{C}_1 - \overline{\boldsymbol{C}}_{p.g.})^{-1} : (\overline{\boldsymbol{C}}_{p.g.} - \boldsymbol{C}_0) \tag{4.25}$$

with $\boldsymbol{C}_1$, $\boldsymbol{C}_0$ and $\overline{\boldsymbol{C}}_{p.g.}$ the stiffness matrix of the inclusions, matrix and pseudo-grain, respectively.

2.3 Numerical homogenization of the pseudo-grain

Each pseudo-grain has been computed within the first step homogenization procedure. Still each one of them is expressed in its own local frame. The second step, as already explained before, will require to express those UD pseudo-grain homogenized properties in the global frame of the aggregate in order to correctly sum them up.

The macro response of an homogenized UD pseudo-grain in its local frame can be expressed through the compliance matrix $[\bar{S}]$ in terms of the following macro engineering constants :

$$\begin{pmatrix} \bar{\varepsilon}_{11} \\ \bar{\varepsilon}_{22} \\ 2\bar{\varepsilon}_{12} \end{pmatrix} = \begin{pmatrix} \frac{1}{\bar{E}_1} & \frac{-\bar{\nu}_{12}}{\bar{E}_1} & 0 \\ \frac{-\bar{\nu}_{21}}{\bar{E}_2} & \frac{1}{\bar{E}_2} & 0 \\ 0 & 0 & \frac{1}{\bar{G}_{12}} \end{pmatrix} \begin{pmatrix} \bar{\sigma}_{11} \\ \bar{\sigma}_{22} \\ \bar{\sigma}_{12} \end{pmatrix} \tag{4.26}$$

for which the inverse gives the following stiffness matrix $[\bar{Q}]$:

$$\begin{pmatrix} \bar{\sigma}_{11} \\ \bar{\sigma}_{22} \\ \bar{\sigma}_{12} \end{pmatrix} = \frac{1}{1 - \bar{\nu}^2_{12}\frac{\bar{E}_2}{\bar{E}_1}} \begin{pmatrix} \bar{E}_1 & \bar{E}_2\bar{\nu}_{12} & 0 \\ \bar{E}_1\bar{\nu}_{21} & \bar{E}_2 & 0 \\ 0 & 0 & \bar{G}_{12} \end{pmatrix} \begin{pmatrix} \bar{\varepsilon}_{11} \\ \bar{\varepsilon}_{22} \\ 2\bar{\varepsilon}_{12} \end{pmatrix} \tag{4.27}$$

Transformation Matrices

To express those matrices in the global frame, we need some tools. Remember that the stiffness and compliance matrices represent fourth-order symmetric tensors. This is to express them in the global axis, we use the following transformation rule :

$$[\bar{S}_{\phi,i}] = [T_\varepsilon]^{-1}[S][T_\sigma] \tag{4.28}$$

$$[\bar{Q}_{\phi,i}] = [T_\sigma]^{-1}[S][T_\varepsilon] \tag{4.29}$$

with

$$[T_\sigma] = \begin{pmatrix} m^2 & n^2 & 2mn \\ n^2 & m^2 & -2mn \\ -mn & mn & (m^2 - n^2) \end{pmatrix} \quad [T_\varepsilon] = \begin{pmatrix} m^2 & n^2 & mn \\ n^2 & m^2 & -mn \\ -2mn & 2mn & (m^2 - n^2) \end{pmatrix}$$

where $m = \cos\phi_i$ and $n = \sin\phi_i$[2]. The notation ϕ_i stands for the pseudo-grain orientation within the aggregate.

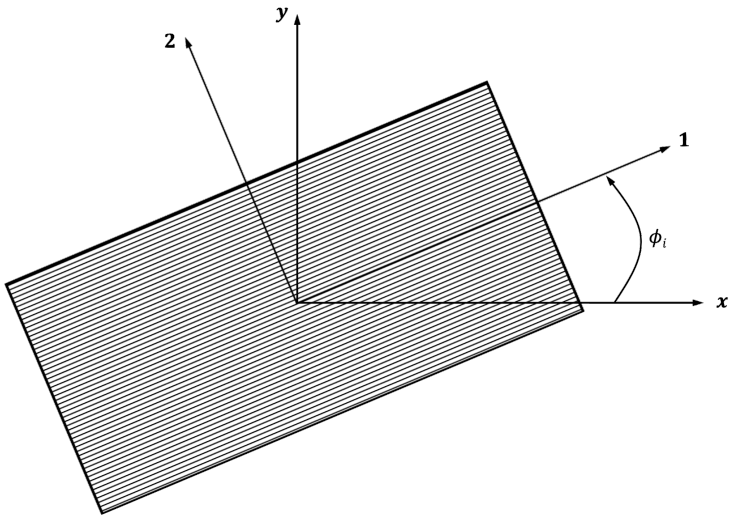

Figure 4.8: Orientation of an homogenized pseudo-grain inside the global frame

3 Matrix with misaligned short fibers, with cavities

3.1 Direct FE analysis on RVE

To compare the models once again we need reference results. To do so we modeled RVE using Digimat-FE. The RVE is 180 by 180 with the same fiber aspect ratio of 24 we used previously. The fiber length is 24 and the diameter of the cavities is fixed at 8. Some examples of such RVEs are depicted on figures 4.9a to 4.9d in the particular case of $v_f = 16\%$ and $v_p = 4\%$. The meshes are for all of them around 132500 CPE3 and CPE4 elements. Fibers are modeled by simple ellipsoids. Results will be given in what follows.

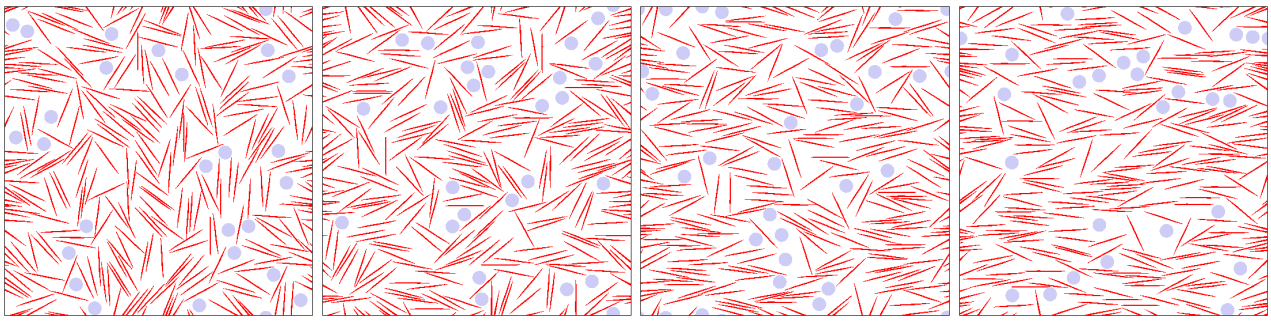

(a) $a_{11} = 0.5$ (b) $a_{11} = 0.6$ (c) $a_{11} = 0.7$ (d) $a_{11} = 0.8$

Figure 4.9: Several microstructures of RVE with misaligned fibers of volume fraction $v_f = 16\%$ and a porosity $v_p = 4\%$, as function of the orientation tensor $\boldsymbol{a}$.

[2] Note that the inverse of $[T_\varepsilon]$ and $[T_\sigma]$ are obtain replacing the angle ϕ_i by $-\phi_i$.

3.2 Two-step method with three-phase PGs

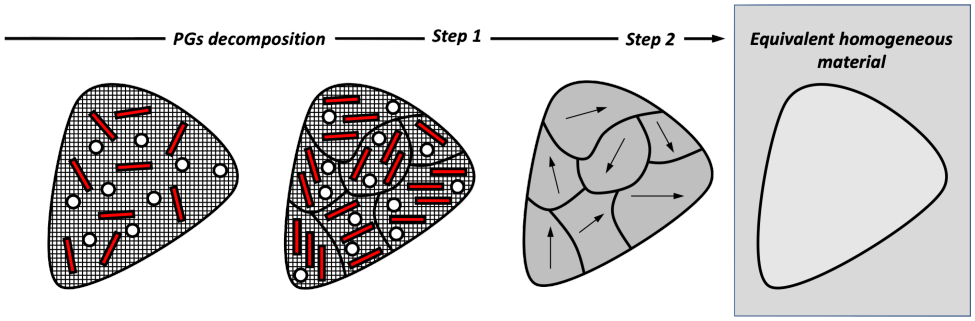

Figure 4.10: Two-step method. First step : UD three-phase PGs decomposition. Step 2 : homogenization of the aggregate composed of the homogenized UD three-phase PGs. The homogenization of this material gives the final equivalent homogeneous material.

3.2.1 First step : homogenization of each three-phase UD pseudo-grain

In the case of a matrix with misaligned short fibers with cavities, each PG is made of a matrix material reinforced with fibers oriented in the same direction and cylindrical cavities where the fibers have the same shape and aspect ratio.

This times, during the first step, each PG is a three-phase composite which contains the same volume fraction of matrix as in RVE, v_0, those inclusions of volume fraction $1 - v_0$ and cavities of volume fraction v_p. The effective engineering properties of the PG are obtained by FEA on the UD unit cell of section 2.2 in chapter 2.

3.2.2 Second step : homogenization of the aggregate

In this second step we follow exactly the same procedure as in the case of no porosity, considering the RVE as an aggregate of homogenized PG (i). Each grain (i) is also characterized by a stiffness $\overline{\boldsymbol{C}}_{i,\boldsymbol{p}}$ computed by FEA during the first step and an orientation tensor $\boldsymbol{p}$. Once again, the PG effective properties are weighted by an orientation distribution function $\psi(\boldsymbol{p})$. The three homogenization methods we considered in the non porous case are used here in the same way except we did before exact for the FE-MT method that need to be reconsidered regarding the porosity of the composite. For this reason, only the latter model is presented in what follows. See section 2 for FE-Voigt and FE-Reuss models.

3.3 Two-step method combined with two-level decomposition

One last method we want to carry out is the combination of the two-step method (section 3.2) with the two-level decomposition (section 1.2). We follow the same procedure we described on related section except that in this case the pseudo-grains are homogenized following a two-level decomposition. In other words, we use results from section 2.3 from chapter 3 for the step 1. Once again, the second step uses FE-Voigt, FE-Reuss and FE-MT as homogenization methods.
The last procedure intents to decompose the first step into two levels :

- Deep level : Contains the matrix and cavities phases. We homogenize it with direct FEA.
- High level : We add aligned fibers to the matrix composed of the homogenized material from the deep level.

At the end of the day we obtain the desired pseudo-grain to be used for the classical second step using once again Voigt, Reuss and direct M-T models. We will focus on the latter scheme because when we consider three-phase PGs, taking into account some porosity, we can show that the model inspired by Mori-Tanaka we introduced in section 2.2.2 is no longer valid. However we can use the following solution.

First we define two strain concentration tensors, one for the fibers, denoted "f", and an other one for the cavities, denoted "c". For the sake of clarity we don't derive the following equations considering N families of fiber (i) but only one family, i.e. $i = 1$:

$$\langle \boldsymbol{\varepsilon} \rangle_{\omega^f_{\boldsymbol{p}_{(k)}}} = \boldsymbol{B}^f_{\boldsymbol{p}^{(k)}} : \langle \boldsymbol{\varepsilon} \rangle_{\omega^0_{\boldsymbol{p}_{(k)}}} \tag{4.30}$$

$$\langle \boldsymbol{\varepsilon} \rangle_{\omega^c_{\boldsymbol{p}_{(k)}}} = \boldsymbol{B}^c_{\boldsymbol{p}^{(k)}} : \langle \boldsymbol{\varepsilon} \rangle_{\omega^0_{\boldsymbol{p}_{(k)}}} \tag{4.31}$$

where using the same assumption of equation 4.10 inspired from Mori-Tanaka. We can derive the expression for the average stain and stress tensors within the RVE ω :

$$\langle \boldsymbol{\varepsilon} \rangle_\omega = v_0 \langle \boldsymbol{\varepsilon} \rangle_{\omega_0} + \sum_{k=1}^{K} \left(v_f \langle \boldsymbol{\varepsilon} \rangle_{\omega^f_{\boldsymbol{p}_{(k)}}} + v_c \langle \boldsymbol{\varepsilon} \rangle_{\omega^c_{\boldsymbol{p}_{(k)}}} \right) W_{\boldsymbol{p}^{(k)}} \tag{4.32}$$

$$\langle \boldsymbol{\sigma} \rangle_\omega = v_0 \boldsymbol{C} \langle \boldsymbol{\varepsilon} \rangle_{\omega_0} + \sum_{k=1}^{K} \left(v_f \langle \boldsymbol{C}^f : \boldsymbol{\varepsilon} \rangle_{\omega^f_{\boldsymbol{p}_{(k)}}} \right) W_{\boldsymbol{p}^{(k)}} \tag{4.33}$$

taking the equations of the strain concentration tensors here above into account. Each on those is composed of UD isotropic linear elastic fibers with a matrix and circular cavities. It means that the strain concentration tensor of the cavity phase $\boldsymbol{B}^c_{\boldsymbol{p}_{(k)}}$ is independent of the orientation of the PG and so the stiffness matrix of the fibers $\boldsymbol{C}^f$.

$$\langle \boldsymbol{\varepsilon} \rangle_\omega = \left[v_0 \boldsymbol{I} + \sum_{k=1}^{K} (v_f \boldsymbol{B}^f_{\boldsymbol{p}^{(k)}} + v_c \boldsymbol{B}^c_{\boldsymbol{p}^{(k)}}) W_{\boldsymbol{p}^{(k)}} \right] : \langle \boldsymbol{\varepsilon} \rangle_{\omega_0} \tag{4.34}$$

$$\langle \boldsymbol{\sigma} \rangle_\omega = \left[v_0 \boldsymbol{C}_0 + \sum_{k=1}^{K} (v_f \boldsymbol{C}^f : \boldsymbol{B}^f_{\boldsymbol{p}^{(k)}}) W_{\boldsymbol{p}^{(k)}} \right] : \langle \boldsymbol{\varepsilon} \rangle_{\omega_0} \tag{4.35}$$

where $W_{\boldsymbol{p}^{(k)}}$ is the weight and K the number of PGs. Finally we can compute the overall stiffness matrix :

$$\overline{\boldsymbol{C}} = \left[v_0 \boldsymbol{C}_0 + \sum_{k=1}^{K} (v_f \boldsymbol{C}^f : \boldsymbol{B}^f_{\boldsymbol{p}^{(k)}}) W_{\boldsymbol{p}^{(k)}} \right] : \left[v_0 \boldsymbol{I} + \sum_{k=1}^{K} (v_f \boldsymbol{B}^f_{\boldsymbol{p}^{(k)}} + v_c \boldsymbol{B}^c_{\boldsymbol{p}^{(k)}}) W_{\boldsymbol{p}^{(k)}} \right]^{-1} \tag{4.36}$$

Note that the strain concentration tensors are computed from two cells, with fiber and void volume fractions of the current considered case. For $\boldsymbol{B}^f_{\boldsymbol{p}^{(k)}}$ we consider an UD cell composed by aligned fibers embedded in a matrix. The tensor is computed from the overall stiffness matrix $\overline{\boldsymbol{C}}^{comp.}$ of the composite using the same equation 4.25 we derived before. In the case of $\boldsymbol{B}^c$, we can prove without given the prove that

$$\boldsymbol{B}^c = -\frac{v_0}{v_c} (\overline{\boldsymbol{C}}^c)^{-1} : (\overline{\boldsymbol{C}}^c - \boldsymbol{C}_0) \tag{4.37}$$

where $\overline{\boldsymbol{C}}^c$ is the overall stiffness of a cell composed of a matrix phase with cavities.

4 Parametric study

4.1 SFRC without cavities

Firstly we study 2-step procedure using Voigt, Reuss and MT models using FE computations for a composites composed only of a matrix and inclusion phases, without porosity and compare those with FE RVE. The results are depicted on figures 4.13 to 4.18. RVEs generated by Naili et al. (2019) have been generated only for values of parameter a ranging 0.5 to 0.8.

FE-MT is surprisingly not really bounded by FE-Voigt and FE-Reuss. This is not what we expected. While v_f is increasing, FE-MT overestimates more and more. FE-MT gives rather good results for $\overline{E}_1^*$, $\overline{E}_2^*$ and $\overline{\nu}_{12}^*$. Moreover, when v_p is increasing FE-MT moves away from FE-Voigt.

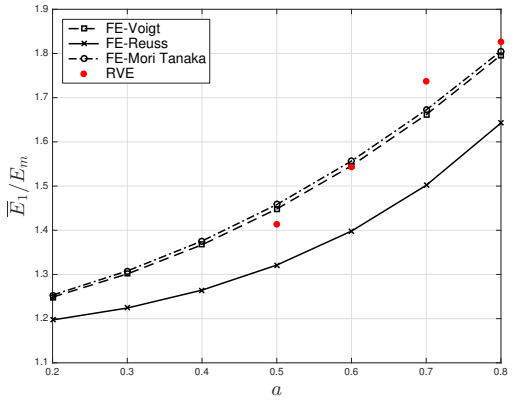

Figure 4.11: Two step homogenization $\overline{E}_1^*$ results compared to RVE results ($v_f = 10\%$).

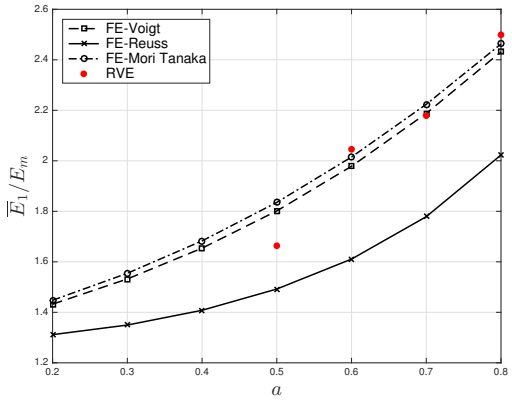

Figure 4.12: Two step homogenization $\overline{E}_1^*$ results compared to RVE results ($v_f = 16\%$).

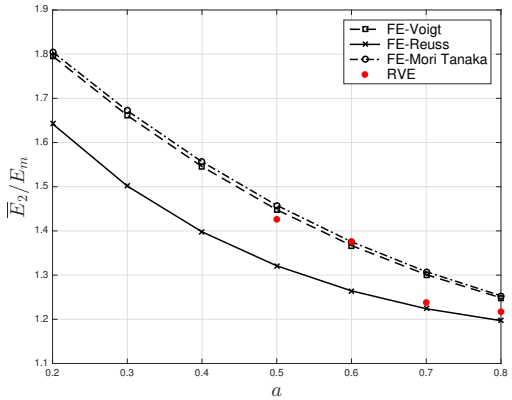

Figure 4.13: Two step homogenization $\overline{E}_2^*$ results compared to RVE results ($v_f = 10\%$).

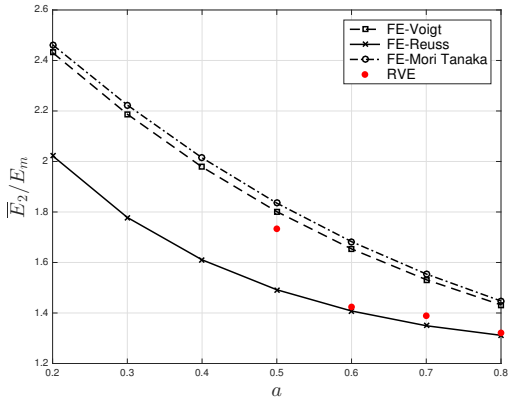

Figure 4.14: Two step homogenization $\overline{E}_2^*$ results compared to RVE results ($v_f = 16\%$).

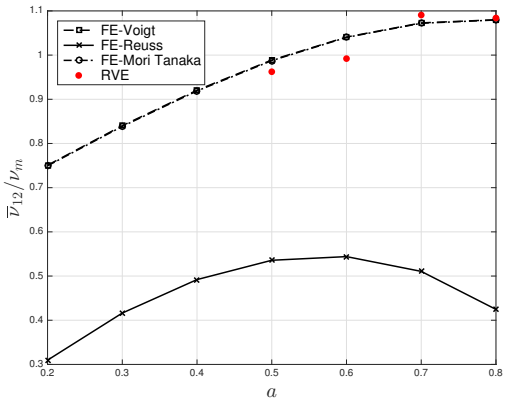

Figure 4.15: Two step homogenization $\overline{\nu}^*_{12}$ results compared to RVE results ($v_f = 10\%$).

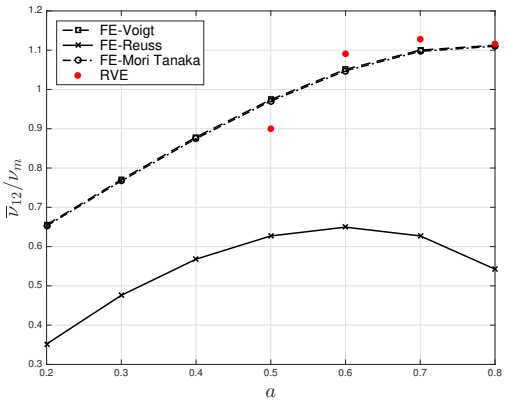

Figure 4.16: Two step homogenization $\overline{\nu}^*_{12}$ results compared to RVE results ($v_f = 16\%$).

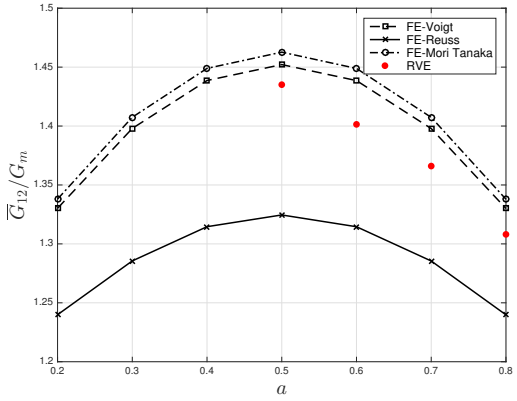

Figure 4.17: Two step homogenization $\overline{G}^*_{12}$ results compared to RVE results ($v_f = 10\%$).

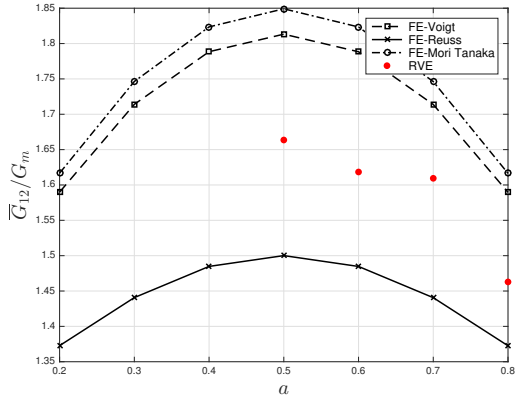

Figure 4.18: Two step homogenization $\overline{G}^*_{12}$ results compared to RVE results ($v_f = 16\%$).

4.2 SFRC with cavities

Now we consider the porous composites composed of a matrix and inclusion phases with some porosity. We introduced above homogenization techniques which we will compare here : a 2-step method using direct FE of the whole composite (2S) and a 2-step method using a 2-level decomposition in step 1 (2S2L). In both methods we use and compare three homogenization methods during step 2 : FE-Voigt, FE-Reuss and FE-MT. For the sake of better visibility regarding the results, we will compare both methods for a particular study case, say $v_f = 16\%$ with $v_p = 4\%$, following Figures 4.19 to 4.26 to RVE's results. The error comitted by each model with respect to RVE reference results are given in table 4.2. Note that $\overline{\nu}^*_{12}$ is not given in the latter table, just by clarity.

We can see that FE-MT is entirely bounded by the FE-Voigt and FE-Reuss only for the 2S homogenization procedure to predict $\overline{E}^*_1$ and $\overline{E}^*_2$. For the latter engineering constant, 2S with FE-MT even gives results close to RVE. This is not the case when using the 2S2L approach. On the other hand for an unknown reason FE-MT gives extremely poor results for $\overline{G}^*_{12}$ when using the 2S method. In both two-step methods, FE-Reuss generally gives results less close to the RVE compared to FE-Voigt and FE-MT, expect for $\overline{E}^*_2$.

We can take a closer look to results given by both two-step procedures for $\overline{E}_1^*$ and $\overline{E}_2^*$. For $\overline{E}_1^*$ we can observe that for misaligned fibers oriented with a_{11} ranging 0.5 to 0.8, i.e. the fibers are more and more aligned with respect to the x-axis, results for FE-Voigt are going closer to RVE while with a_{11} ranging 0.5 to 0.1, i.e. the fibers are more and more aligned with respect to the y-axis, results for FE-Reuss are closer to RVE. When we look at $\overline{E}_2^*$, this is exactly the same reasoning but in this case, FE-Reuss is closer to RVE for a_{11} ranging 0.5 to 0.8 while FE-Voigt is closer the RVE for a_{11} ranging 0.5 to 0.1. Around $a_{11} = 0.5$ we can see that FE-MT is the best homogenization method.

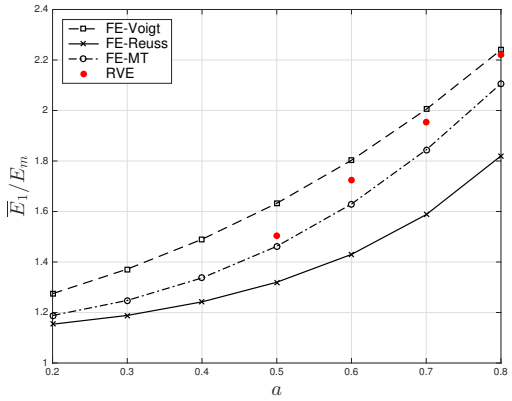

Figure 4.19: $\overline{E}_1^*$: 2S method vs. RVE ($v_f = 16\%$, $v_p = 4\%$).

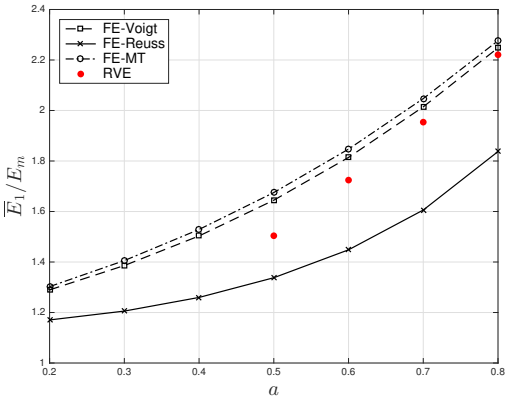

Figure 4.20: $\overline{E}_1^*$: 2S2L method vs. RVE ($v_f = 16\%$, $v_p = 4\%$).

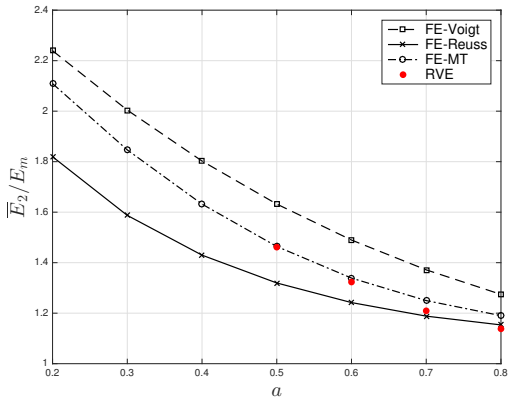

Figure 4.21: $\overline{E}_2^*$: 2S method vs. RVE ($v_f = 16\%$, $v_p = 4\%$).

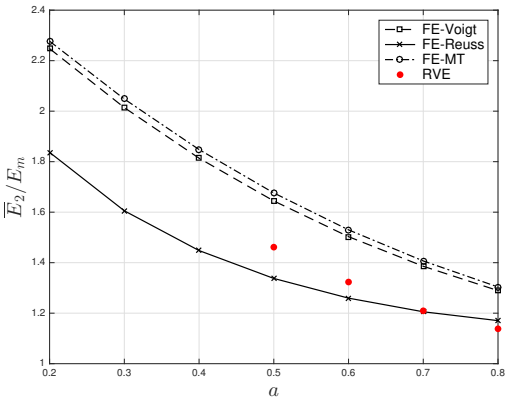

Figure 4.22: $\overline{E}_2^*$: 2S2L method vs. RVE ($v_f = 16\%$, $v_p = 4\%$).

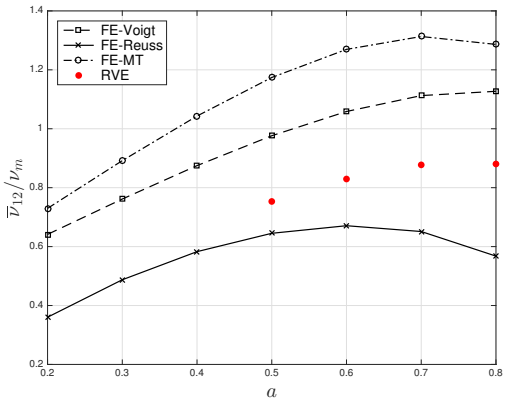

Figure 4.23: $\overline{\nu}^*_{12}$: 2S method vs. RVE ($v_f = 16\%$, $v_p = 4\%$).

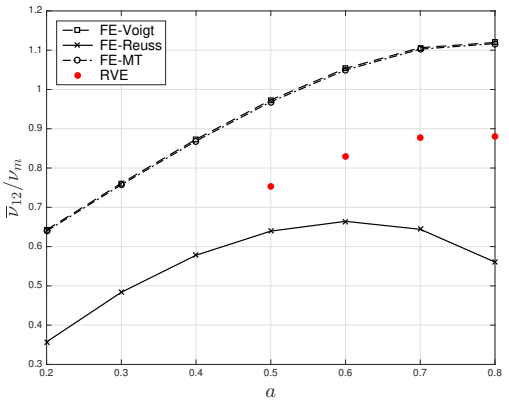

Figure 4.24: $\overline{\nu}^*_{12}$: 2S2L method vs. RVE ($v_f = 16\%$, $v_p = 4\%$).

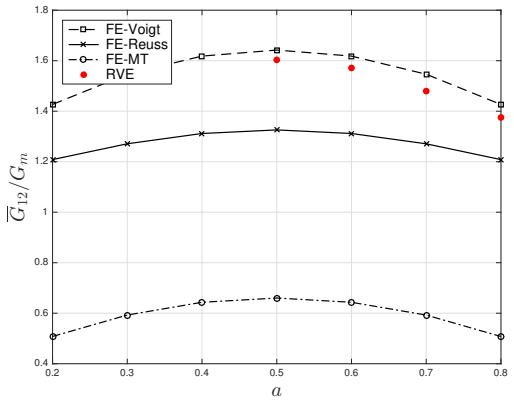

Figure 4.25: $\overline{G}^*_{12}$: 2S method vs. RVE ($v_f = 16\%$, $v_p = 4\%$).

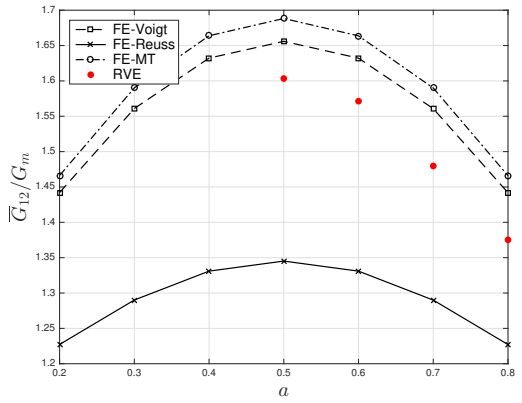

Figure 4.26: $\overline{G}^*_{12}$: 2S2L method vs. RVE ($v_f = 16\%$, $v_p = 4\%$).

a_{11}	Method	$\overline{E}_{1,r}$ [%]	$\overline{E}_{1,MT}$ [%]	$\overline{E}_{1,V}$ [%]	$\overline{E}_{2,r}$ [%]	$\overline{E}_{2,MT}$ [%]	$\overline{E}_{2,V}$ [%]	$\overline{G}_{12,r}$ [%]	$\overline{G}_{12,MT}$ [%]	$\overline{G}_{12,V}$ [%]
0.5	2S	12.24	2.78	8.54	9.7	0.19	11.68	17.3	58.83	2.42
	2S2L	11.05	11.38	9.36	8.48	11.38	9.36	16.1	5.3	3.28
0.6	2S	17.07	5.49	4.56	6.15	1.18	12.56	16.52	59.06	2.98
	2S2L	16.01	7.12	5.21	4.82	7.12	5.21	15.3	5.88	3.87
0.7	2S	18.74	5.62	2.6	1.74	3.35	13.42	14.11	59.95	4.5
	2S2L	17.81	4.78	3.1	0.31	4.78	3.1	12.82	7.45	5.48
0.8	2S	18.04	5.15	0.87	1.35	4.57	11.97	12.14	63.07	3.73
	2S2L	17.26	2.5	1.23	2.84	2.5	1.23	10.77	6.6	4.84

Table 4.2: Results with the two-step method with three phases in step 1 (2S) and two-step method using a two-level decomposition in step 1 (2S2L). Plane stress results for $v_f = 16\%$ and $v_p = 4\%$.

Chapter 5

Conclusion

In this work we proposed several finite element homogenization procedures for porous short-fiber reinforced composites and compare them with direct finite element analysis in order to investigate the best way to homogenize such materials. First of all we studied and modeled unit cells with aligned UD fibers and no porosity to ensure accuracy of the composite overall properties when using FE homogenization method under plane stress and plane strain assumption. Based on 2D RVEs homogenization results we concluded an excellent agreement between both models, i.e. FE homogenization using UD unit cell provides accurate results.

By direct FEA we studied the influence of the porosity on the properties of the composite and used a two-level decomposition of a porous aligned SFRC to conclude with excellent agreements between the homogenization using direct FEA on a UD unit cell and the two-level decomposition homogenization method.

We followed this work with the study of misaligned porous SFRCs. On the one hand we considered a basic non-porous aligned SFRC and compared FE homogenization results on RVE we found in the literature with predictions of the overall mechanical properties using three different two-step homogenization procedures. In a first step we used aforementioned results we performed on FE UD unit cell and in a second step we homogenized the aggregate by means of Voigt, Reuss and inspired Mori-Tanaka methods only using FE results. On the other hand we considered porous misaligned SFRCs and also performed the three above-mentioned two-step procedures : first using direct FE UD unit cell results in step 1, secondly using a two-level decomposition based on previous FE results. In the case of two-phase misaligned SFRCs we encountered unexpected results as the FE-MT homogenization were not bounded by FE-Voigt and FE-Reuss as expected. However, FE-MT did followed RVE results, close to FE-Voigt. The analyses of porous misaligned SFRCs show that using the two-step homogenization procedure with direct FEA on UD unit cell containing all the three phases is better than using a two-level decomposition during the first step of the homogenization.

This work was performed assuming linear elasticity for the matrix material. Further investigations can be done using more realistic matrix material, e.g. assuming an elasto-plastic matrix material. We also assumed both cylindrical identical inclusions and circular cavities (in 2D), we could evaluate the macroscopic response of such porous SFRC using different shapes of inclusions and voids to model, for instance, more realistic micro-cracks inside the composite.

Bibliography

Abaqus (2019). *General-Purpose Finite Element Software.* ABAQUS Inc., Pawtucket, RI, USA.

Aboudi, J. (1991). *Mechanics of Composite Materials: A Unified Micromechanical Approach (Studies in Applied Mechanics).* Elsevier Science.

Aboudi, J., Arnold, S. M., and Bednarcyk, B. A. (2012). *Micromechanics of Composite Materials: A Generalized Multiscale Analysis Approach.* Butterworth-Heinemann.

Advani, S. and Hsiao, K.-T. (2012). 1 - introduction to composites and manufacturing processes. In Advani, S. G. and Hsiao, K.-T., editors, *Manufacturing Techniques for Polymer Matrix Composites (PMCs)*, Woodhead Publishing Series in Composites Science and Engineering, pages 1 – 12. Woodhead Publishing.

Advani, S. G. and Tucker, C. L. (1987). The use of tensors to describe and predict fiber orientation in short fiber composites. *Journal of Rheology*, 31(8):751–784.

Benveniste, Y. (1987). A new approach to the application of mori-tanaka's theory in composite materials. *Mechanics of Materials*, 6(2):147 – 157.

Böhm, H. J. (January 2019). A short introduction to basic aspects of continuum micromechanics.

Choren, J., Heinrich, S., and Silver-Thorn, B. (2013). Young's modulus and volume porosity relationships for additive manufacturing applications. *Journal of Materials Science*, 48:5103–5112.

Doghri, I. (2000). *Micro-mechanics of materials*, pages 519–544. Springer Berlin Heidelberg, Berlin, Heidelberg.

Doghri, I. (2000b). *Two-dimensional problems in Cartesian coordinates*, pages 163–191. Springer Berlin Heidelberg, Berlin, Heidelberg.

Doghri, I. (2010). *Mechanics of Deformable Solids: Linear, Nonlinear, Analytical and Computational Aspects.* Springer.

Doghri, I. (2018). *Lecture notes : Mechanics of Composite Materials.* Institute of Mechanics, Materials and Civil Engineering (IMMC), Université catholique de Louvain, Louvain-la-Neuve, Belgium.

Doghri, I. and Friebel, C. (2005). Effective elasto-plastic properties of inclusion-reinforced composites. study of shape, orientation and cyclic response. *Mechanics of Materials*, 37(1):45 – 68.

Duschlbauer, D., Böhm, H. J., and Pettermann, H. E. (2006). Computational simulation of composites reinforced by planar random fibers: Homogenization and localization by unit cell and mean field approaches. *Journal of Composite Materials*, 40(24):2217–2234.

Eshelby, J. D. and Peierls, R. E. (1957). The determination of the elastic field of an ellipsoidal inclusion, and related problems. *Proceedings of the Royal Society of London. Series A. Mathematical and Physical Sciences*, 241(1226):376–396.

Ghossein, E. and Lévesque, M. (2012). A fully automated numerical tool for a comprehensive validation of homogenization models and its application to spherical particles reinforced composites. *International Journal of Solids and Structures*, 49(11):1387 – 1398.

Kang, G.-Z. and Gao, Q. (2002). Tensile properties of randomly oriented short δ-al2o3 fiber reinforced aluminum alloy composites: Ii. finite element analysis for stress transfer, elastic modulus and stress–strain curve. *Composites Part A: Applied Science and Manufacturing*, 33(5):657 – 667.

Kouznetsova, V. G. (2018). *Lecture notes : Computational Homogenization*. Department of Mechanical Engineering, Eindhoven University of Technology Eindhoven, The Netherlands.

Lejeunes, S. and Bourgeois, S. (2011). Une Toolbox Abaqus pour le calcul de propriétés effectives de milieux hétérogènes. In *10e colloque national en calcul des structures*.

Lielens, G., Pirotte, P., Couniot, A., Dupret, F., and Keunings, R. (1998). Prediction of thermomechanical properties for compression moulded composites. *Composites Part A: Applied Science and Manufacturing*, 29(1):63 – 70. Selected Papers Presented at the Fourth International Conference on Flow Processes in Composite Material.

Liu, S.-J. (2012). 2 - injection molding in polymer matrix composites. In Advani, S. G. and Hsiao, K.-T., editors, *Manufacturing Techniques for Polymer Matrix Composites (PMCs)*, Woodhead Publishing Series in Composites Science and Engineering, pages 15 – 46. Woodhead Publishing.

Lubachevsky, B. D. and Stillinger, F. H. (1990). Geometric properties of random disk packings. *Journal of Statistical Physics*, 60(5):561–583.

Lubachevsky, B. D., Stillinger, F. H., and Pinson, E. N. (1991). Disks vs. spheres: Contrasting properties of random packings. *Journal of Statistical Physics*, 64(3):501–524.

Mori, T. and Tanaka, K. (1973). Average stress in matrix and average elastic energy of materials with misfitting inclusions. *Acta Metallurgica*, 21(5):571 – 574.

Naili, C., Doghri, I., Kanit, T., Suckiman, S., Aissa Berraies, A., and Imad, A. (2019). Elastic short fiber composites: unbiased full-field evaluation of various homogenization methods (still in preparation). *ZAMM - Journal of Applied Mathematics and Mechanics / Zeitschrift für Angewandte Mathematik und Mechanik*.

Nemat-Nasser and Hori, M. (1993). *Micromechanics: overall properties of heterogeneous solids*. Elsevier Science.

Ogierman, W. and Kokot, G. (2017). Homogenization of inelastic composites with misaligned inclusions by using the optimal pseudo-grain discretization. *International Journal of Solids and Structures*, 113-114:230 – 240.

Pierard, O. (2006). *Micromechanics of inclusion-reinforced composites in elasto-plasticity and elasto-viscoplasticity : modeling and computation*. PhD thesis, Université catholique de Louvain.

Pierard, O., Friebel, C., and Doghri, I. (2004). Mean-field homogenization of multi-phase thermo-elastic composites: a general framework and its validation. *Composites Science and Technology*, 64(10):1587 – 1603.

Prakash, R. (1981). Significance of defects in the fatigue failure of carbon fibre reinforced plastics. *Fibre Science and Technology*, 14(3):171 – 181.

Reuss, A. (1929). Berechnung der fließgrenze von mischkristallen auf grund der plastizitätsbedingung für einkristalle . *ZAMM - Journal of Applied Mathematics and Mechanics / Zeitschrift für Angewandte Mathematik und Mechanik*, 9(1):49–58.

Rintoul, M. D. and Torquato, S. (1997). Reconstruction of the structure of dispersions. *Journal of Colloid and Interface Science*, 186(2):467 – 476.

Voigt, W. (1889). Ueber die beziehung zwischen den beiden elasticitätsconstanten isotroper körper. *Annalen der Physik*, 274(12):573–587.

Wu, W., Owino, J., Al-Ostaz, A., and Cai, L. (2014). Applying periodic boundary conditions in finite element analysis. In *Simulia (Abaqus) Community Conference, Providence, RI*.

Zaoui, A. (2002). Continuum micromechanics: Survey. *Journal of Engineering Mechanics*, 128(8):808–816.

UNIVERSITÉ CATHOLIQUE DE LOUVAIN
École polytechnique de Louvain
Rue Archimède, 1 bte L6.11.01, 1348 Louvain-la-Neuve, Belgique | **www.uclouvain.be/epl**